FINAL TECHNICAL REPORT

AWARD NUMBER: G14AP00110

Constraining shallow subsurface S wave velocities with the initial portion of local P waves recorded at multiple seismic networks including ANSS and EarthScope Transportable Array in the CEUS.

Principal Investigator(s):

Mehrdad Hosseini, Paul Somerville, Andreas Skarlatoudis, Hong Kie Thio, and Jeff Bayless

URS Group, Inc.
300 S Grand Ave
Los Angeles, CA 90071

August 10, 2016

"Research supported by the U.S. Geological Survey (USGS), Department of the Interior, under USGS award number G14AP00110. The views and conclusions contained in this document are those of the authors and should not be interpreted as necessarily representing the official policies, either expressed or implied, of the U.S. Government."

ABSTRACT

USARRAY and ANSS seismic stations provide an invaluable waveform dataset for studying ground motion attenuation in the Central and Eastern United States. However, the dataset is useful only after the site effects at each station are well understood. Since there are many stations in USARRAY and ANSS, it would be costly to accurately determine sub-surface velocity structure beneath every station using geophysical exploration techniques involving arrays, such as ReMi and SASW. It would be more economical to estimate the site effects with waveforms recorded at the seismic stations. Such approaches have been widely applied, but most of them involve the frequency dependent ratio between the horizontal and vertical component of either ambient noise or S waves from earthquakes. The horizontal component of P waves can also be used to infer sub-surface velocity structure. It is demonstrated that the ratio of radial to vertical P waves is mostly sensitive to sub-surface shear velocity, so the radial/vertical ratio of the P wave is a good indicator of subsurface shear velocity. Therefore, the subsurface velocity structure can be estimated using an approach similar to teleseismic P receiver functions, but at much smaller scale and higher frequency that matches well with results from ReMi and Refraction/Reflection techniques (Ni et al. 2014). We used the approach introduced by Ni et al. (2014) and calibrated our models with findings from Ni and Somerville (2013) to obtain data on shallow shear-wave structure in the Central and Eastern United States. A rich database of local earthquakes from 2009 to 2013 recorded at ~560 seismic stations was analyzed and associated receiver functions were inverted. The results are in reasonable agreement with local geology and with the results of Ni and Somerville (2013), Ni et al. (2014) and Kim et al. (2014). The data are made publically available for future refinement.

Contents

Introduction

The database of strong motion recordings in the Central and Eastern United States (CEUS) is too sparse to permit the development of empirical ground motion prediction models. However, the Earthscope Transportable Array (USARRAY) and ANSS stations provide a vast amount of waveform data of earthquakes in the Central and Eastern United States (CEUS). Since January 1st, 2009, hundreds of M2.5 or larger earthquakes have occurred in the study area. These abundant waveforms will be very helpful in developing ground motion prediction models if the recording site responses can be characterized. Invasive geophysical exploration methods such as down hole or cross hole measurement are the most accurate way of determining subsurface velocities beneath target site, but they are too costly and in some cases, non-uniqueness obscures the realistic attributes of the subsurface (Hosseini and Pezeshk, 2015). Less costly, noninvasive array-based methods such as SASW and ReMi are also widely applied in studying site response. However, the Earthscope Transportable Array alone has about 400 broadband stations, and investigating the site responses of so many stations with these methods would be costly and time consuming. In this situation, single station-based methods are more readily applicable because these methods only require waveform data recorded at that particular station.

Three component local P waves can be used to constrain subsurface velocity structure, in a way similar to the method of teleseismic P receiver functions (Ni et al. 2014). Typically, P waves-based methods are more robust because P waves are the first arrival and feature high signal to noise ratio, unlike the S waves which could be contaminated by P coda at high frequencies. Results from this study can be used to reduce the uncertainties in source and path effect studies as described by Hosseini et al. (2015).

We used ground motions from local earthquakes from 2009 through 2013 recorded on multiple seismic networks to constrain shallow shear wave velocities in the CEUS. To make sure that underlying assumptions of converted phases at the boundary of sedimentary basin, necessary for a receiver function study is valid, we limited the magnitude range of seismic events from 2.5 to 4.5 moment magnitude (Ni et al., 2014). The locations of the stations and earthquakes range from the Appalachian Highlands and Atlantic Plain Provinces in the east to the western boundary of the Interior Plain Province. Waveforms are recorded by broadband stations from multiple seismic networks including the Transportable Array (TA), New Madrid (NM), CERI Southern Appalachian (ET), International Miscellaneous Stations (IM), United States (US), Global Seismograph (IU), United States National (US), and Lamont-Doherty Cooperative (LD) seismic networks. The majority of stations are from Transportable Array. Figure 1 is from USArray website showing the schedule and location of this network.

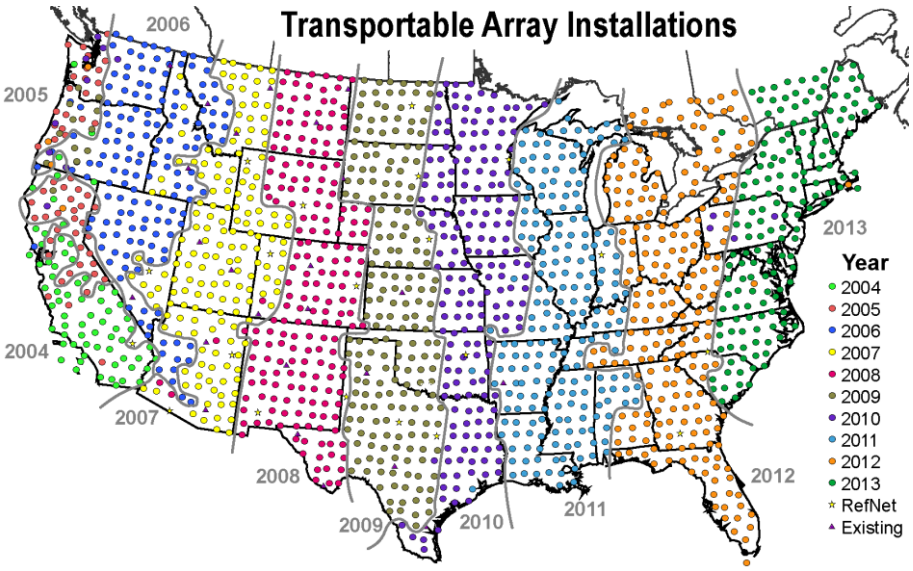

Figure 1. Transportable Array (TA) stations install plan and location in the United States. Source: USArray website, last accessed March 2016).

Table 1. List of seismic networks and seismic stations used in this study.

*	Station	*	Station	*	Station	*	Station	*	Station	*	Station	*	Station
1	CPCT	82	153A	163	K31A	244	Q45A	325	T30A	406	V37A	487	X56A
2	FPAL	83	154A	164	K43A	245	Q46A	326	T31A	407	V38A	488	Y22D
3	SWET	84	155A	165	KMSC	246	Q47A	327	T32A	408	V39A	489	Y23A
4	UOM1	85	221A	166	KSCO	247	Q49A	328	T33A	409	V40A	490	Y24A
5	UOM2	86	224A	167	L29A	248	Q50A	329	T34A	410	V41A	491	Y25A
6	UOM3	87	225A	168	L30A	249	Q51A	330	T35A	411	V42A	492	Y26A
7	UOM4	88	226B	169	L31A	250	Q52A	331	T36A	412	V43A	493	Y27A
8	TKL	89	227A	170	L44A	251	Q53A	332	T37A	413	V44A	494	Y28A
9	TX31	90	228A	171	L53A	252	Q54A	333	T38A	414	V45A	495	Y29A
10	CCM	91	229A	172	M31A	253	Q55A	334	T39A	415	V46A	496	Y30A
11	SSPA	92	230A	173	M44A	254	Q57A	335	T40A	416	V47A	497	Y32A
12	WCI	93	231A	174	M52A	255	R21A	336	T41A	417	V48A	498	Y33A
13	WVT	94	232A	175	M54A	256	R22A	337	T42A	418	V49A	499	Y34A
14	ACCN	95	233A	176	MSTX	257	R23A	338	T43A	419	V50A	500	Y35A
15	BMNY	96	234A	177	N23A	258	R24A	339	T44A	420	V51A	501	Y36A
16	BRNY	97	236A	178	N31A	259	R25A	340	T45A	421	V52A	502	Y37A
17	FLET	98	237A	179	N32A	260	R26A	341	T46A	422	V53A	503	Y38A
18	FRNY	99	240A	180	N44A	261	R27A	342	T47A	423	V54A	504	Y39A
19	HBVT	100	241A	181	N45A	262	R38A	343	T48A	424	W23A	505	Y40A
20	HCNY	101	248A	182	N46A	263	R39A	344	T49A	425	W24A	506	Y41A
21	KSPA	102	324A	183	N50A	264	R40A	345	T50A	426	W25A	507	Y42A
22	LUPA	103	325A	184	N51A	265	R41A	346	T51A	427	W26A	508	Y43A
23	MCVT	104	326A	185	N52A	266	R42A	347	T52A	428	W27A	509	Y46A
24	MMNY	105	329A	186	N53A	267	R43A	348	T53A	429	W29A	510	Y47A
25	MSNJ	106	330A	187	N54A	268	R44A	349	T54A	430	W30A	511	Y48A

26	MVL	107	331A	188	N55A	269	R45A	350	T55A	431	W31A	512	Y49A
27	NCB	108	332A	189	O27A	270	R46A	351	T56A	432	W32A	513	Y50A
28	NPNY	109	333A	190	O28A	271	R47A	352	T57A	433	W33A	514	Y51A
29	ODNJ	110	334A	191	O29A	272	R48A	353	T58A	434	W34A	515	Y52A
30	PAL	111	335A	192	O30A	273	R49A	354	TASO	435	W35A	516	Y53A
31	PANJ	112	336A	193	O31A	274	R50A	355	TUL1	436	W36A	517	Y54A
32	POTS	113	341A	194	O32A	275	R51A	356	U21A	437	W37A	518	Y55A
33	PTN	114	425A	195	O43A	276	R52A	357	U22A	438	W37B	519	Z22A
34	WCNY	115	426A	196	O44A	277	R53A	358	U23A	439	W38A	520	Z24A
35	WVNY	116	428A	197	O47A	278	R54A	359	U24A	440	W39A	521	Z25A
36	BLO	117	429A	198	O49A	279	R55A	360	U25A	441	W40A	522	Z26A
37	CGM3	118	430A	199	O50A	280	R57A	361	U26A	442	W41A	523	Z27A
38	CLTN	119	431A	200	O51A	281	R58B	362	U27A	443	W41B	524	Z28A
39	FVM	120	432A	201	O52A	282	S21A	363	U28A	444	W42A	525	Z29A
40	GLAT	121	433A	202	O53A	283	S22A	364	U31A	445	W45A	526	Z30A
41	GNAR	122	434A	203	O54A	284	S23A	365	U32A	446	W46A	527	Z31A
42	HALT	123	435B	204	O55A	285	S24A	366	U33A	447	W47A	528	Z32A
43	HBAR	124	526A	205	O56A	286	S25A	367	U34A	448	W48A	529	Z33A
44	HENM	125	527A	206	P23A	287	S26A	368	U35A	449	W49A	530	Z34A
45	HICK	126	532A	207	P24A	288	S27A	369	U36A	450	W50A	531	Z35A
46	LNXT	127	534A	208	P25A	289	S28A	370	U37A	451	W51A	532	Z36A
47	LPAR	128	632A	209	P27A	290	S31A	371	U38A	452	W52A	533	Z37A
48	MGMO	129	735A	210	P29A	291	S32A	372	U39A	453	W53A	534	Z39A
49	OLIL	130	833A	211	P30A	292	S33A	373	U40A	454	W54A	535	Z40A
50	PARM	131	835A	212	P31A	293	S34A	374	U41A	455	WHTX	536	Z41A
51	PBMO	132	934A	213	P32A	294	S35A	375	U42A	456	X23A	537	Z42A
52	PEBM	133	ABTX	214	P38A	295	S36A	376	U43A	457	X24A	538	Z48A
53	PENM	134	BGNE	215	P40A	296	S38A	377	U44A	458	X25A	539	Z49A
54	PLAL	135	D51A	216	P41A	297	S39A	378	U44B	459	X26A	540	Z50A
55	PVMO	136	D52A	217	P42A	298	S40A	379	U45A	460	X27A	541	Z51A
56	SIUC	137	D53A	218	P43A	299	S41A	380	U46A	461	X28A	542	Z52A
57	SLM	138	D54A	219	P44A	300	S42A	381	U47A	462	X29A	543	Z53A
58	UALR	139	D55A	220	P45A	301	S44A	382	U48A	463	X30A	544	Z54A
59	USIN	140	D56A	221	P46A	302	S45A	383	U49A	464	X31A	545	Z55A
60	X102	141	E52A	222	P47A	303	S46A	384	U50A	465	X32A	546	Z57A
61	X201	142	E53A	223	P50A	304	S47A	385	U51A	466	X33A	547	ACSO
62	X301	143	E54A	224	P51A	305	S48A	386	U52A	467	X34A	548	AMTX
63	121A	144	F51A	225	P52A	306	S49A	387	U53A	468	X35A	549	BINY
64	123A	145	F52A	226	P53A	307	S50A	388	U54A	469	X36A	550	BLA
65	124A	146	F55A	227	P54A	308	S51A	389	U55A	470	X37A	551	CBN
66	125A	147	G53A	228	P55A	309	S52A	390	U56A	471	X38A	552	JCT
67	126A	148	G55A	229	P56A	310	S53A	391	V21A	472	X39A	553	LONY
68	127A	149	G57A	230	Q22A	311	S54A	392	V22A	473	X40A	554	LRAL
69	128A	150	H25A	231	Q23A	312	S55A	393	V23A	474	X41A	555	MIAR
70	129A	151	H55A	232	Q24A	313	S57A	394	V24A	475	X42A	556	MNTX
71	130A	152	H56A	233	Q25A	314	S58A	395	V25A	476	X43A	557	NCB
72	131A	153	H58A	234	Q26A	315	SFIN	396	V26A	477	X44A	558	OXF
73	133A	154	I27A	235	Q29A	316	T22A	397	V27A	478	X46A	559	SDCO
74	134A	155	I28A	236	Q31A	317	T23A	398	V28A	479	X47A	560	TZTN

75	135A	156	I55A	237	Q32A	318	T24A	399	V30A	480	X48A	561	WMOK
76	136A	157	J27A	238	Q39A	319	T24B	400	V31A	481	X49A		
77	137A	158	J28A	239	Q40A	320	T25A	401	V32A	482	X50B		
78	140A	159	J30A	240	Q41A	321	T26A	402	V33A	483	X51A		
79	143A	160	J31A	241	Q42A	322	T27A	403	V34A	484	X52A		
80	151A	161	K22A	242	Q43A	323	T28A	404	V35A	485	X53A		
81	152A	162	K30A	243	Q44A	324	T29A	405	V36A	486	X54A		

* Station numbers and seismic networks are color code based on the following scheme map:

ET	IM	IU	LD	NM	TA	US

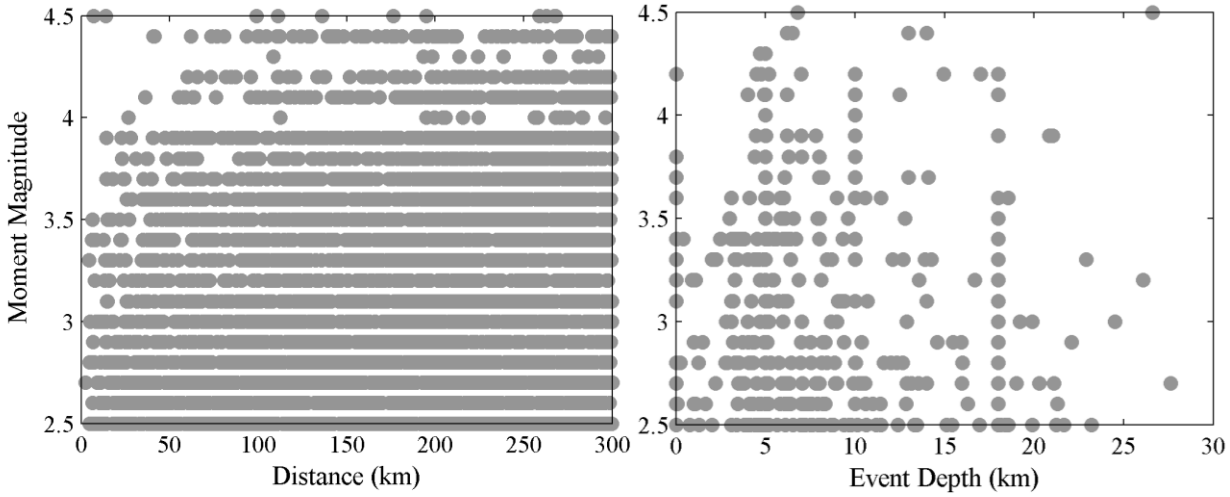

Figure 2. Moment Magnitudes of recorded events are plotted with distance (left) and focal depth (right).

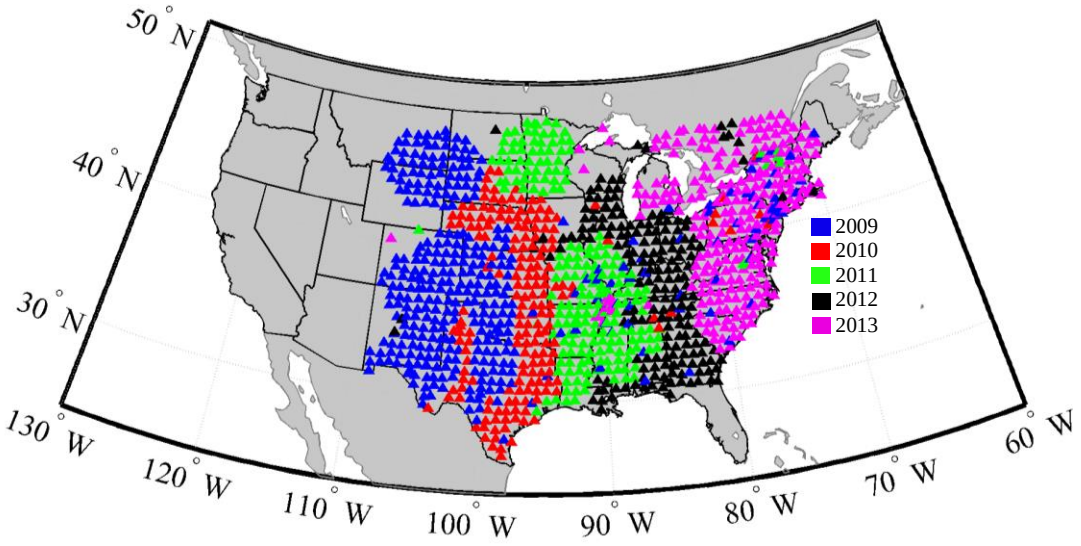

Figure 3. A total of 561 unique stations recorded a total of ~3000 earthquakes in the desired distance and magnitude ranges used in this study. Different colors present the stations deployed in a specific year. A total of ~73300 three-component recordings were gathered and analyzed in this study. A list of stations is provided in Table 1 and a map of the earthquakes is presented in Figure 4.

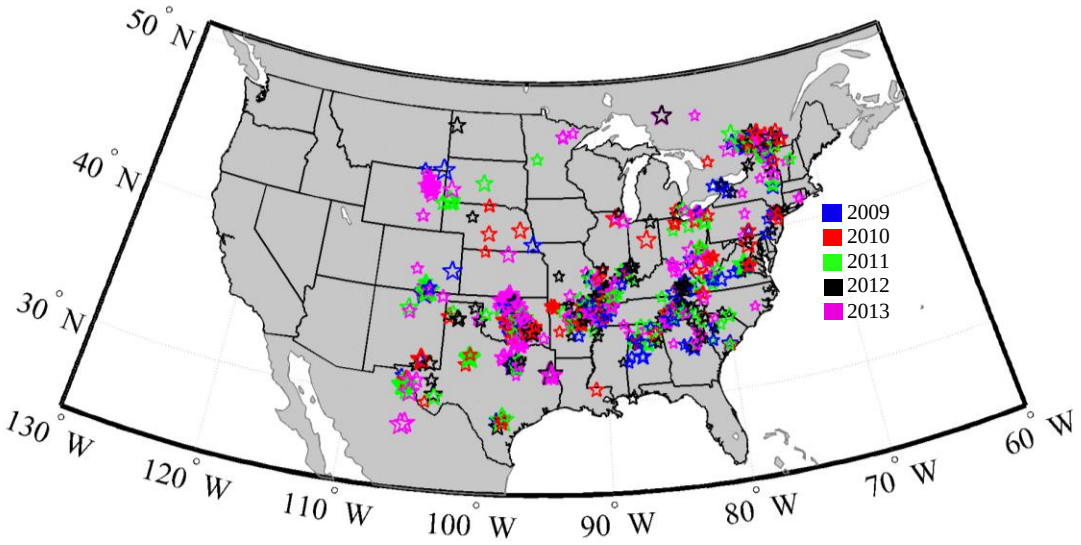

Figure 4. A total of ~3000 Earthquakes are used in this study, covering the Central and Eastern United States from 2009 to 2013. Different colors present events occurring in a specific year.

Processing

Processing of raw data was performed in a way consistent with our methodology of receiver function determination. We removed the instrument response from raw data and high-pass filtered the corrected recordings. We then used an automatic arrival time detection procedure to detect the onset of the earliest P wave phase. Regarding the sensitivity of the detection algorithm to signal to noise ratio (SNR), we visually inspected the detected arrivals by comparing them with theoretical arrival times. In the next step, we excluded those recordings where the time difference between the first and second P wave phases was less than 0.7 seconds to avoid phase interference, and used the appropriate ray parameter in the deconvolution process to obtain the receiver functions at each station from multiple events.

Prior to the stacking of multiple receiver functions at a specific station, we visually inspected the receiver functions and synchronized the receiver functions in time with the one having the highest SNR value prior to stacking. These processes are explained in the following sections.

Instrument Correction

The recorded ground motions were first corrected for the instrument response by performing de-convolution in the frequency domain over a limited frequency band. We band limited the instrument correction process considering that all seismometers have zero response at zero frequency and that low SNR at high frequencies requires response damping. We used a tapered low- and high-pass filter with four sorted corner frequencies ($0<f_1< f_2< f_3< f_4$) [f_1=0.2 f_2=0.21] for the high-pass filter and [f_3=0.95 f_{nyq} f_4=0.96 f_{nyq}] for the low-pass filter. The filter applied between [f_1 and f_2] and [f_3 and f_4] is a quarter cycle of a cosine wave. These filter parameters are selected in a manner that preserves the overall properties of the waveform and allows a stable deconvolution to be performed. Figure 5 and Figure 6 show the instrument-

corrected recordings at station MGMO from 7 June 2011 and 27 November 2009 earthquakes. The first earthquake has a higher SNR than the second one.

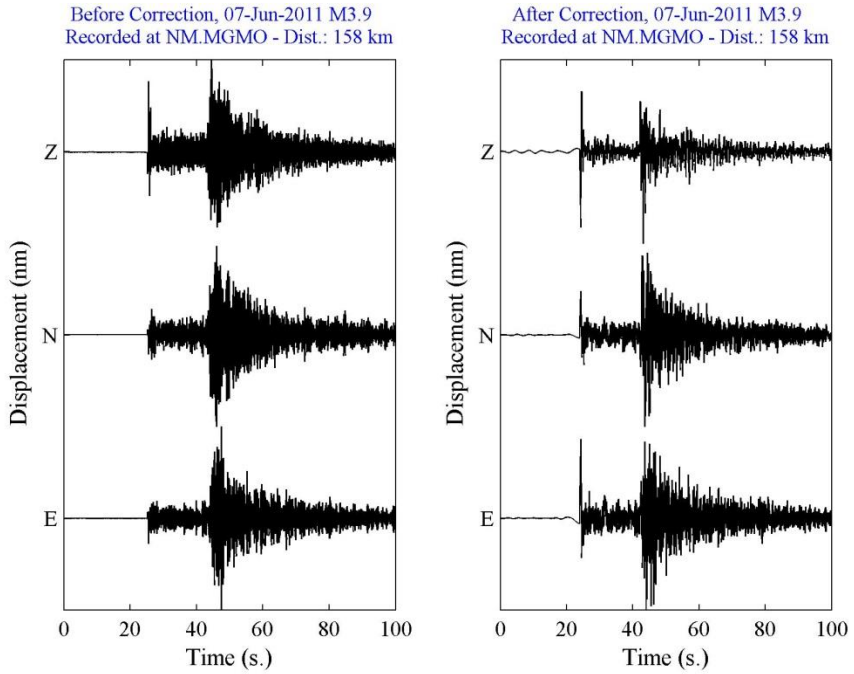

Figure 5. Three-component recordings at MGMO station, before (left) and after (right) instrument-correction for the 7 June 2011 earthquake. These recordings have a high signal to noise ratio.

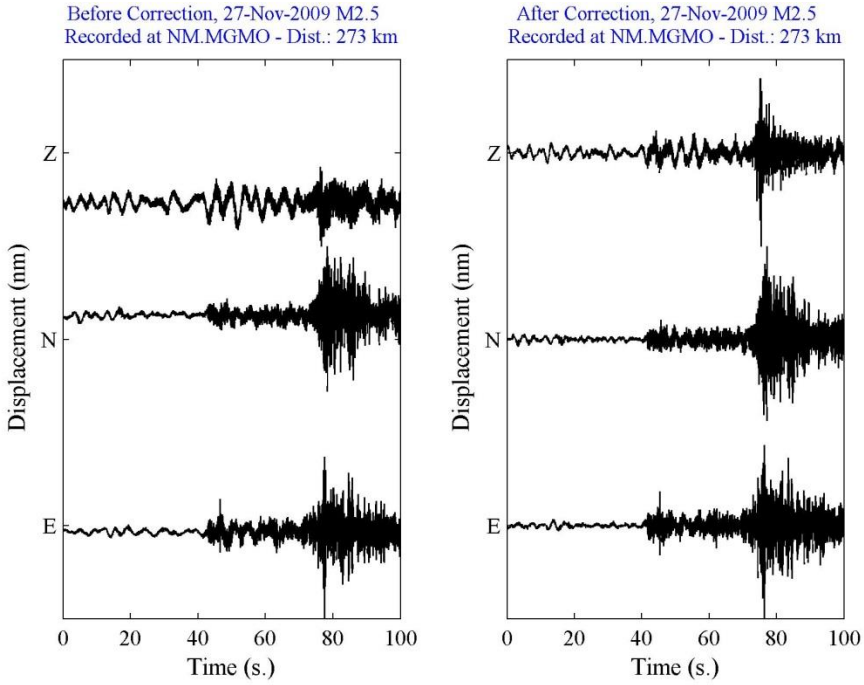

Figure 6. Three-component recordings at MGMO station, before (left) and after (right) instrument-correction for the 27 November 2009 earthquake. These recordings have a lower signal to noise ratio compared to that in Figure 5.

High-Pass Filtering of Seismograms

After removing the instrument response, the seismograms were high-pass filtered with a four-pole Butterworth filter with corner frequency of 1 Hz similar to Ni et al. (2014). On most raw seismograms, the long period noise (5 sec or longer) is strong. With high-pass filtering at 1Hz, the noise before the P wave is substantially suppressed, as shown in Figure 7. Some seismograms require higher corner frequencies of 2Hz and 4Hz for high-pass filtering, but the P waveform becomes more complicated at higher frequencies (Ni and Somerville, 2013). Considering the abundant availability of data, we limited the use of such seismograms due to their low signal to noise ratio. An example seismogram with strong low frequency noise is shown in Figure 6. Corrected ground motions are rotated to the great circle path for radial, traverse, and vertical components prior to performing the next step.

Signal to Noise Ratio

Signal to noise ratio is calculated for each component separately by averaging the squared velocity of a recorded ground motion using the following equation from Helmholtz-Centre Potsdam - GFZ German Research Centre for Geosciences used in parallel with the Maeda (1985) P wave arrival detection process:

$$SNR = \frac{\sqrt{2}\max(\mathbf{s}_{[t_O\ t_O+100]})}{\left(\sum_{i=t_O-30}^{t_O-10} s_i^2 \Big/ \frac{30-10}{\Delta_t}\right)^{-\frac{1}{2}}} \quad (1)$$

where s is the waveform signal, t_O denotes the origin time in seconds, and Δ_t is the time step in seconds. The SNR value for each seismic station is used to select high quality receiver functions prior to the manual inspection and the stacking process. We calculated the rms of SNR values of the three components as an indicator of quality of signal recorded at a specific station. At each station, recordings of earthquakes from 2009 to 2013 were sorted based on their SNR value. We neglected recordings with SNR value less than 100 and picked the 15 recordings with the highest SNR for further processing. The SNR for earthquake *i* recorded at station *j* is calculated from three rotated components in the following manner:

$$SNR_{i,j} = \sqrt{\left(SNR_{i,j}^{T}\right)^2 + \left(SNR_{i,j}^{R}\right)^2 + \left(SNR_{i,j}^{Z}\right)^2} \quad (2)$$

The final SNR value representing the quality of signal in station *j* from *n* earthquakes is calculated as:

$$SNR_j = \frac{\sum_{i=1}^{n} SNR_{i,j}}{n} \quad (3)$$

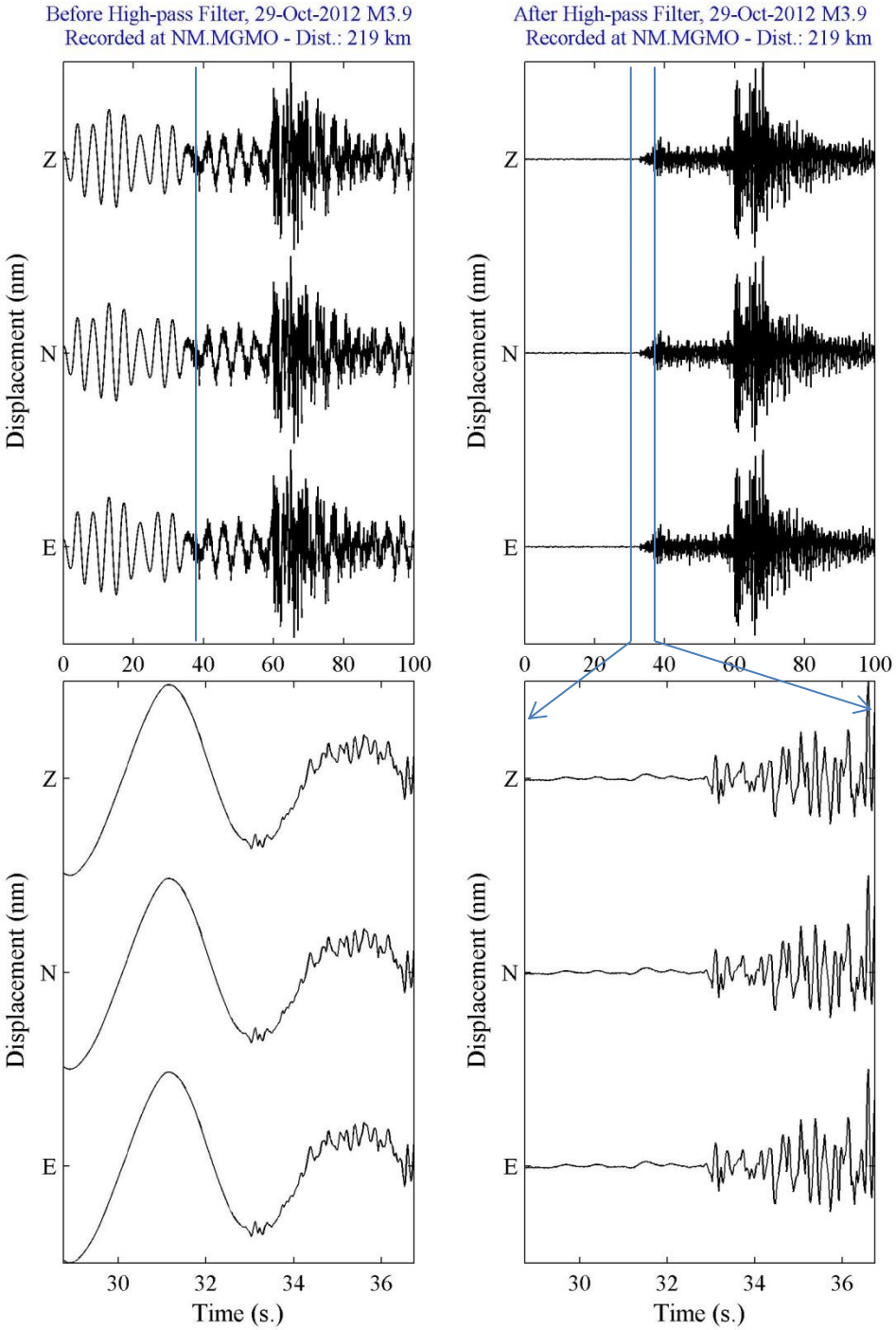

Figure 7. Recorded waveforms at station TA.Y46A from the 29 Oct 2012 earthquake. Instrument-corrected three-component time series are shown before (top left) and after (top right) high-pass filtering with a corner frequency of 1 Hz. In the bottom plots, waveforms are windowed for the P wave arrival for clarity showing the P wave arrival before (bottom left) and after (bottom right) high-pass filtering. This figure shows that high-pass filtering successfully suppressed the long period noise in the data.

Automatic Arrival Time Detection

The receiver functions in this project are from P-waves that are converted to S waves at the sharp boundary between the sediments and the bedrock. For this reason, we windowed the rotated ground motions starting from the P wave arrival, with a five second window length prior to deconvolution for receiver function. Detection of P wave arrivals was performed automatically using the Maeda (1985) approach. Maeda (1985) uses an Akaike information criterion (AIC) picker function that can be calculated directly from the records without fitting them using the autoregressive (AR) process. However, such non-AR AIC pickers are sensitive to the SNR (Zhang et al., 2003). For this reason, we manually inspected every recording for correct P wave arrival time detection and manually picked the P wave arrival time in the case of AIC picker failure. Figure 8 shows examples of identification of P-arrival time using the AR-AIC algorithm. The recorded ground motions are converted to velocity prior to de-convolving the radial components from the vertical ones.

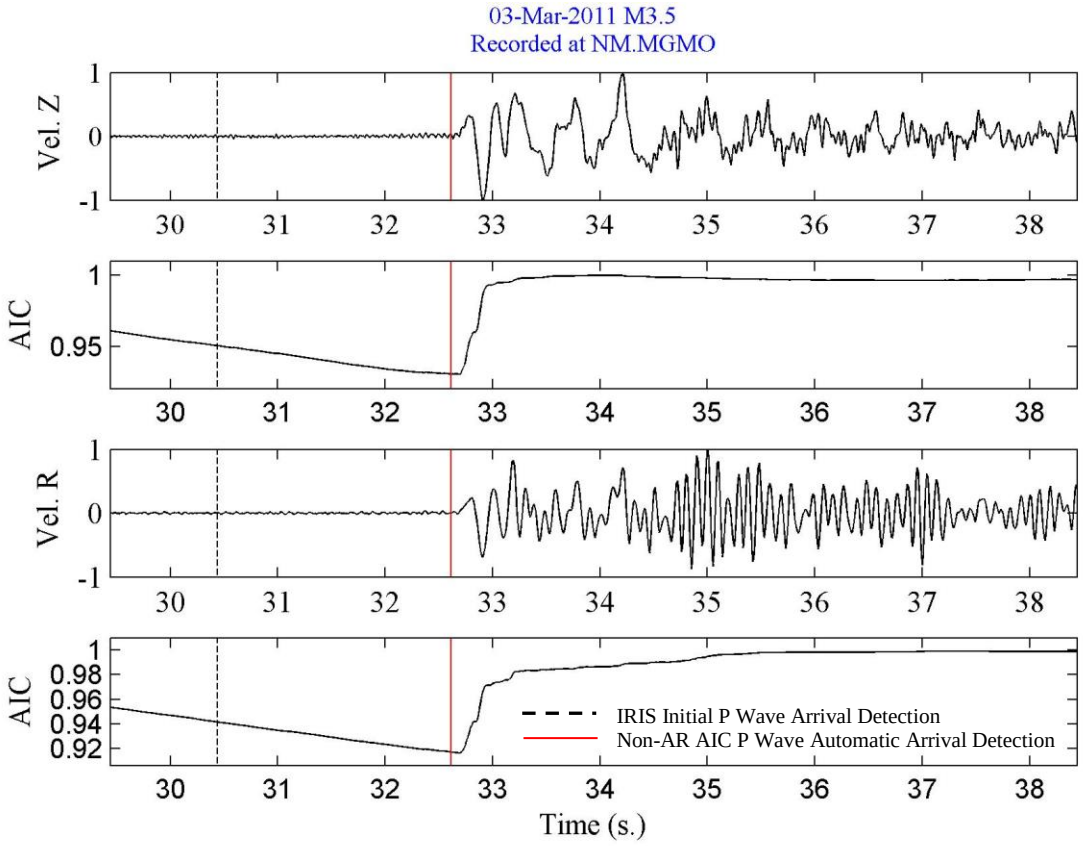

Figure 8. Arrival time detected by the non-AR AIC algorithm used in this study for the 3 March 2011 earthquake recorded at NM.MGMO station. The minimum value of the AIC function determines the arrival time.

Visual Inspection

Visual inspection is performed to make sure that the automatic P wave arrival time is detected correctly. A large number of recordings needed revisions of their P wave arrival times. To make sure that we are picking correct arrival time, we calculated theoretical travel times for various phases of compressional waves which helps detect P wave arrivals robustly. Theoretical arrival times were calculated using the Taup software tool using the Ak135 earth model (Crotwell et al. 1999). In some cases the theoretical first arrival of the P wave matched the observation quite well as shown in Figure 9, and in some cases they differ slightly.

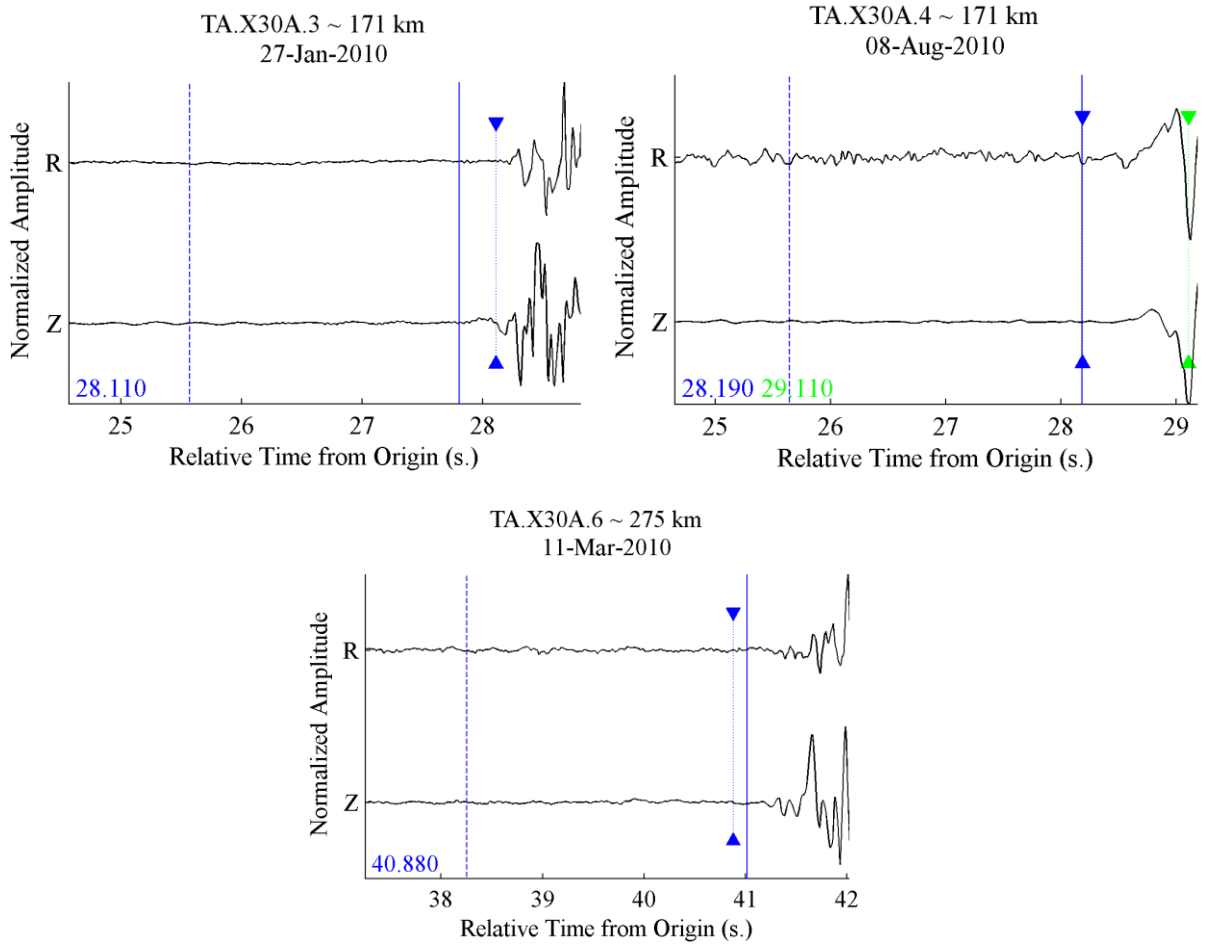

Figure 9. Recordings of three earthquakes at TA.X30A station. The initial arrival time predicted by IRIS or the non-AR AIC picker is shown with the dashed blue line, theoretical arrivals of various P phases predicted using Taup are shown with thin lines with triangles at both ends, and the final manual pick is shown with the solid blue line. The theoretical arrival time using the Ak135 earth model matches the observations well. The time series are normalized velocity records. Colored numbers are theoretical arrival times corresponding to the phase shown with line of the same color and triangles at both ends.

Phase Interference

We calculated theoretical P wave phases to exclude recordings where multiple phases have close arrival times that might negatively affect the reliability of our results. An example is shown in Figure 10 where P wave phases are arriving very close in time. Similar records were excluded from our database of time series; the time differences between the first and seconds P phases were calculated and if they were less than a logical value we excluded the recording. The logical value of the difference between the first two P phase arrivals was selected to be at least ~ 0.8 to 1.0 second and was also confirmed by visual inspection of the dominant period of the recordings. Avoiding phase interference aids picking the ray parameter of the first P wave arrival with confidence in the deconvolution for receiver function.

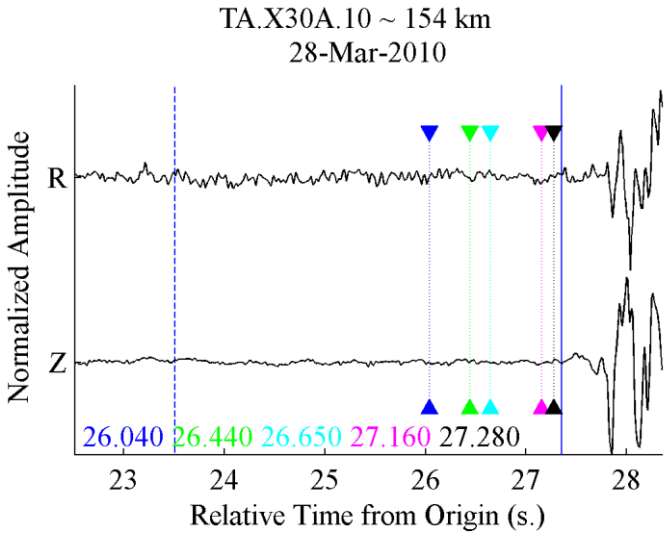

Figure 10. Recordings of 28 March 2010 earthquakes at TA.X30A station, where different phases (presented with thin line with triangles at both ends) interfere. This recording was excluded from the database. Colored numbers are theoretical arrival times corresponding to the phase shown with a line of the same color and triangles at both ends. The initial arrival time predicted by IRIS or the non-AR AIC picker is shown with the dashed blue line and the final manual pick is shown with the solid blue line.

P Wave Receiver Function

Typically P wave-based subsurface imaging methods are more robust because P waves are the first arrival and feature high signal noise ratio, unlike the S waves which could be contaminated by P coda at high frequencies.

For the case of a layer of unconsolidated sediments over bedrock, various converted seismic phases are observed (Sp, or Ps), and are used to improve the velocity structure in the sediments (Chen et al, 1996; Langston, 2003). A similar idea can be used to model very near surface structure using the initial portion

of P waveforms. In Figure 11, the ray paths of the P wave and a converted phase (Ps) are displayed. As most earthquakes occur in crystalline basement where seismic velocities are high, and most stations are situated on material of lower velocities, the incident angles of P and Ps near the seismic station are typically much smaller than the takeoff angle on the fault. Thus intuitively, the P wave is weaker on the radial component than on the vertical component because of the steeper ray path of the P wave, and Ps is stronger on the radial component because its polarization is perpendicular to the ray path (Ni et al., 2014).

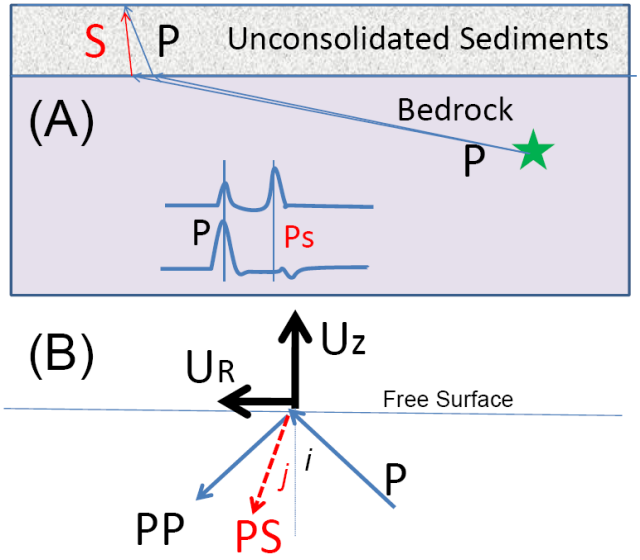

Figure 11. Schematic rays showing interaction of the P wave and subsurface structure (A) and the free surface (B). The radial (top) and vertical (bottom) waveforms are shown in Panel A. Source: Ni et al. (2014).

Mathematical Analysis

The relative amplitude of the radial and vertical components of P waves depends only on the subsurface shear wave velocity and the ray parameter. The ray parameter is determined by structure that is much deeper than the shallow structure that we want to resolve. This is because the actual particle motion due to the interaction of incoming P or S waves with the free surface recorded by a seismic station is different from that of waves propagating in a whole space. The particle motions of incoming P waves at the free surface are described as (Aki and Richards, 2002; Ni et al. 2014):

$$(U_R, U_T, U_Z) = \frac{\left[\frac{4\alpha p}{\beta^2}\frac{\cos i}{\alpha}\frac{\cos j}{\beta}, 0, \frac{-2\alpha}{\beta^2}\frac{\cos i}{\alpha}\left(\frac{1}{\beta^2} - 2p^2\right)\right]}{\left(\frac{1}{\beta^2} - 2p^2\right)^2 + 4p^2\frac{\cos i}{\alpha}\frac{\cos j}{\beta}} \quad (4)$$

where U_R, U_T, U_Z are radial, tangential and vertical components of the particle velocity at the free surface, *i* is the angle between the P ray and the vertical axis, and *j* is the angle between the S ray and the vertical axis (Figure 11B).

Then from equation (1), it is straightforward to obtain the ratio between the radial and vertical components of P waves,

$$\frac{U_R}{U_Z} = \frac{-2\,\beta p\ cosj}{1 - 2p^2\beta^2} \qquad (5)$$

As seen in equation (5), the ratio between radial and vertical components of the incoming P wave depends mostly on the shear velocity and ray parameter. The ratio $\frac{U_R}{U_Z}$ of the P wave is proportional to the sub-surface shear velocity and we will use this fact to resolve the shear wave velocity profile in the CEUS seismograph stations using the inversion of the receiver functions.

In order to show that the ratio U_R/U_Z of the P wave is mostly sensitive to subsurface shear velocity, Ni et al. (2014) computed synthetic seismograms of three component P waves for five different models, which correspond to the five NEHRP site classes (A, B, C, D, E), with average shear wave velocities in the upper 30 meters (V_{S30}) of about 2,150, 1,068, 523, 255 and 125 meters/sec respectively (Figure 12A). In Figure 12B, the radial component for each subsurface model is displayed, and the source duration is chosen to be very short (0.05 second) so that individual seismic phases are isolated from each other. It is obvious that smaller subsurface shear velocity is always associated with smaller P amplitude and larger amplitude of secondary arrivals which could consist of Ps and its multiples. When the source time function is chosen to be 0.1 second (appropriate for M3 earthquakes), a similar pattern can be observed in Figure 12C as in Figure 12B. In both Figures 12B and 12C, the NEHRP site class A model shows the strongest P amplitude and the smallest secondary arrivals.

Although the subsurface shear velocity models affect the radial component of P waves, the vertical component (black traces) is not affected much (left side of Figure 13). From this figure, it is clear that the ratio U_R/U_Z of the P wave is sensitive to subsurface velocity. However, the ratio of radial to vertical component is dependent on ray parameter *p* as presented in equation 5, which is typically not known accurately due to errors in earthquake location, focal depth and/or crustal velocity structure. To investigate the effects of ray parameter on the radial component of P waves, Ni et al. (2014) computed synthetic seismograms for ray parameters from 0.07 to 0.15 s/km. Assuming a half space crustal model with constant P velocity of 6km/s, the difference in ray parameters corresponds to a focal depth difference of about 20km for an earthquake at a distance of 50km. The waveforms on the right side of Figure 13 are very similar, which is not surprising because the radial components of the initial P waves are mostly controlled by shear waves in the top soft layer and the shear waves propagate almost vertically for incoming P waves even though they have different incident angles. The error in ray parameter is probably within 0.08s/km for earthquakes in our study area, because the crustal structure in the CEUS is relatively simple (Ou and Herrmann, 1990) and the relatively dense seismographic station coverage of the seismic networks. Following Ni et al. (2014) and based on the similarity of ray parameters for different stations we stacked receiver functions from various earthquakes for a specific station and used the average value of their ray parameters.

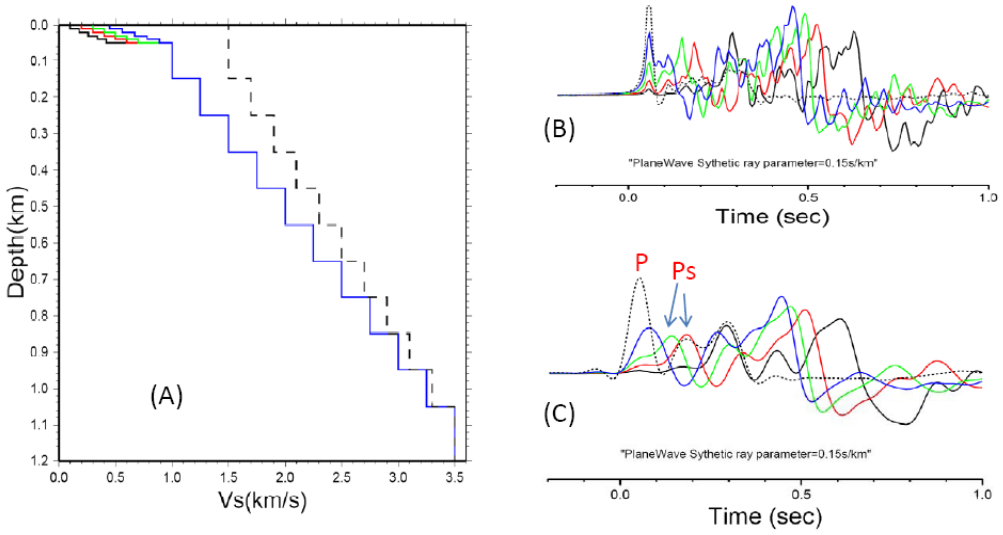

Figure 12. (A) Five shear velocity models corresponding to NEHRP A (dashed black), B (blue), C (green), D (red) and E (solid black) site classes. (B) Corresponding synthetic seismograms of radial components of local P waves, assuming source time duration 0.05 second. (C) Same as (B), but source time duration is 0.1second. Source: Ni et al. (2014)

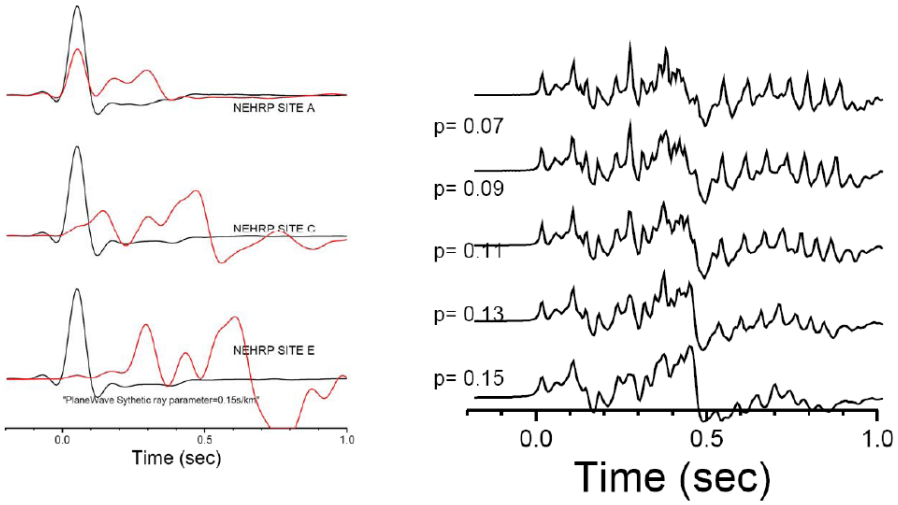

Figure 13. (Left) Comparison of radial (red) and vertical (black) components of local P waves for different NEHRP site categories. On the radial component, the direct P wave is smaller and secondary arrivals are much stronger when the sub-surface shear velocity is smaller. (Right) Radial components for different ray parameter (p). The waveforms are similar for different p. Source: Ni et al. (2014)

Deconvolution

The deconvolution process is an iterative procedure in the time domain described by Ligorria and Ammon (1999). In this method the deconvolution is expressed as a sequence of Gaussian filtered impulses. The zero phase Gaussian filter is defined as

$$H(f) = \exp\left[\left(-\pi f/\bar{\alpha}\right)^2\right] \qquad (6)$$

where parameter $\bar{\alpha}$ controls the frequency content, with the e^{-1} point at a frequency α/π. Thus an $\bar{\alpha}$ = 1. 0 gives a low-pass version of the receiver function at a frequency of about 0.3 Hz (Herrmann 2002). We selected an alpha value of 50 following Ni et al. (2014) for local earthquakes.

Figure 14 shows the radial and vertical components of multiple earthquakes recorded at the MGMO station. The recordings in Figure 14 have been selected as the final recordings for MGMO station where the processing steps mentioned in previous sections have been performed. Figure 15 shows the same data as Figure 14, windowing in the P wave arrival vicinity. In Figures 14 and 15, final arrival time is presented with a solid vertical blue line. Radial and vertical time series are cut 1 and 3 seconds before and after the P wave arrival before deconvolution. The deconvolution is performed in the time domain using the Ligorria and Ammon (1999) procedure where vertical components are de-convolved from radial components. The receiver function, convolved with the vertical component, will result in the radial component. Figure 16 shows the predicted and observed radial component from the deconvolution process.

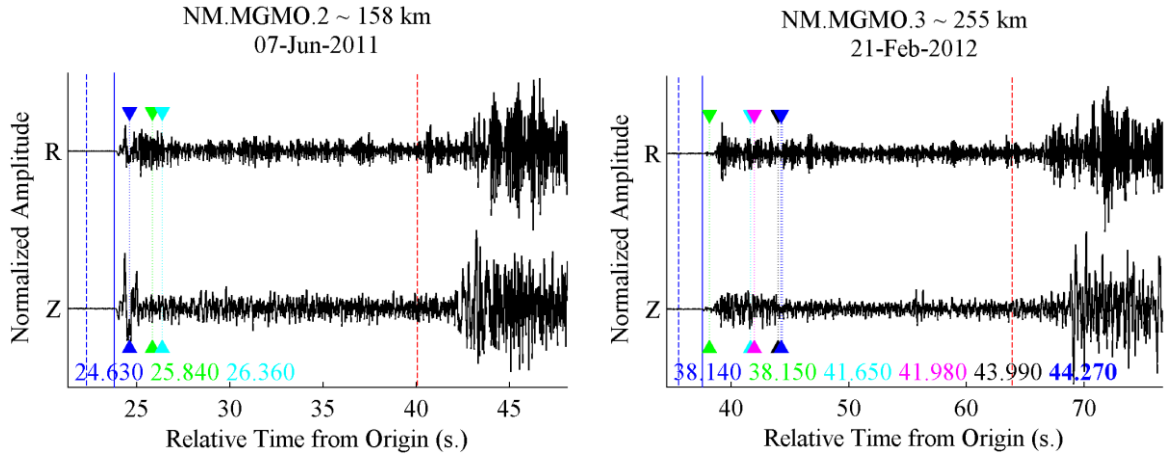

Figure 14. Recordings of 14 earthquakes at NM.MGMO station, sorted based on descending order of SNR. The initial P and S waves' arrival time predicted by IRIS or the non-AR AIC picker are shown with dashed blue and red lines, theoretical arrivals of various P phases predicted using Taup are shown with thin lines with triangles at both ends, and the final manual pick of the P wave arrival is shown with a solid blue line. Theoretical arrival times are calculated using the Ak135 earth model. The time series are normalized velocity records. The title of each plot depicts the name of the seismic network and station, epicentral distance, and earthquake date.

Numbers with different colors are theoretical arrival time in seconds corresponding to the phase shown with the line of the same color and triangles at both ends.

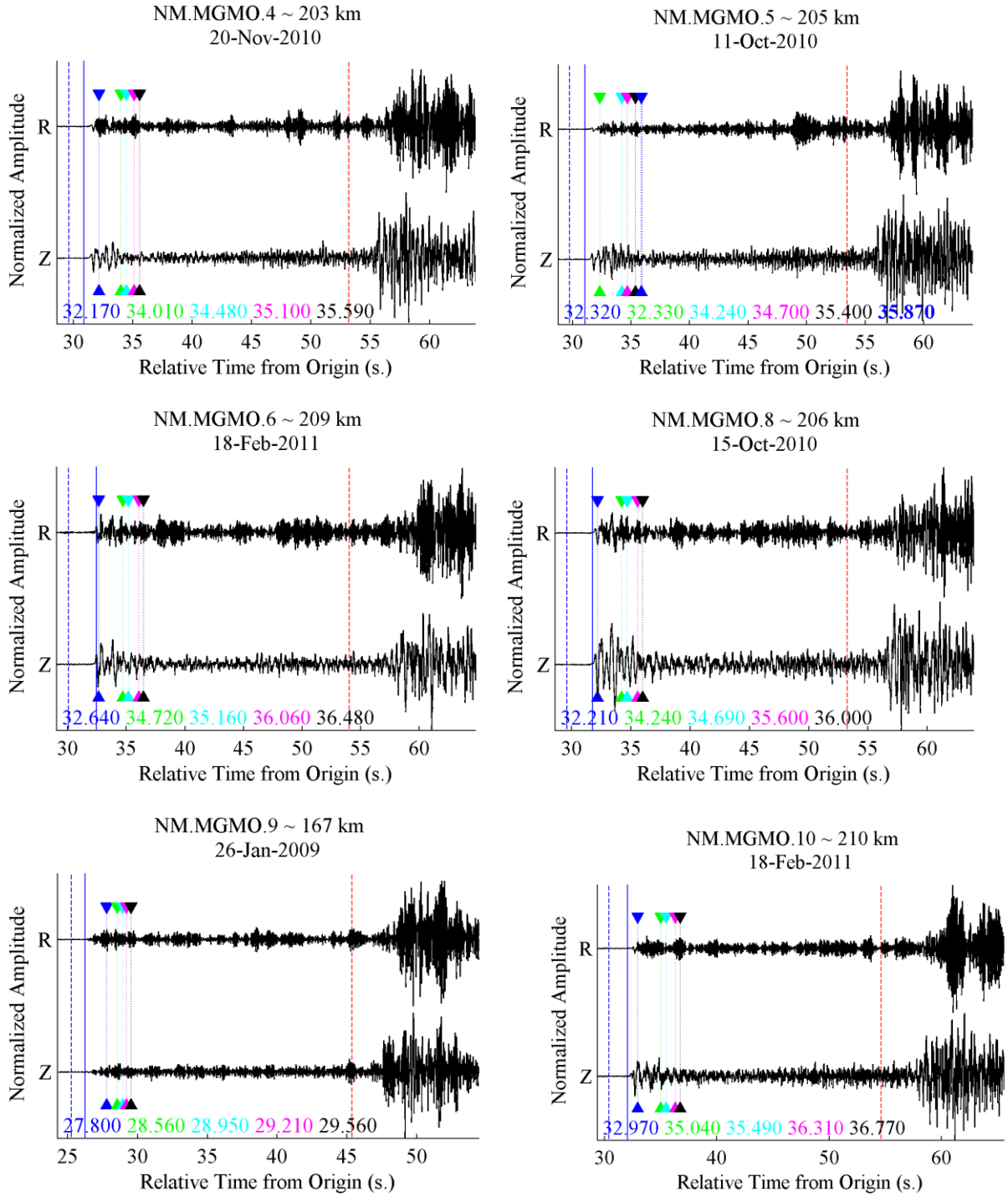

Figure 14. Continued.

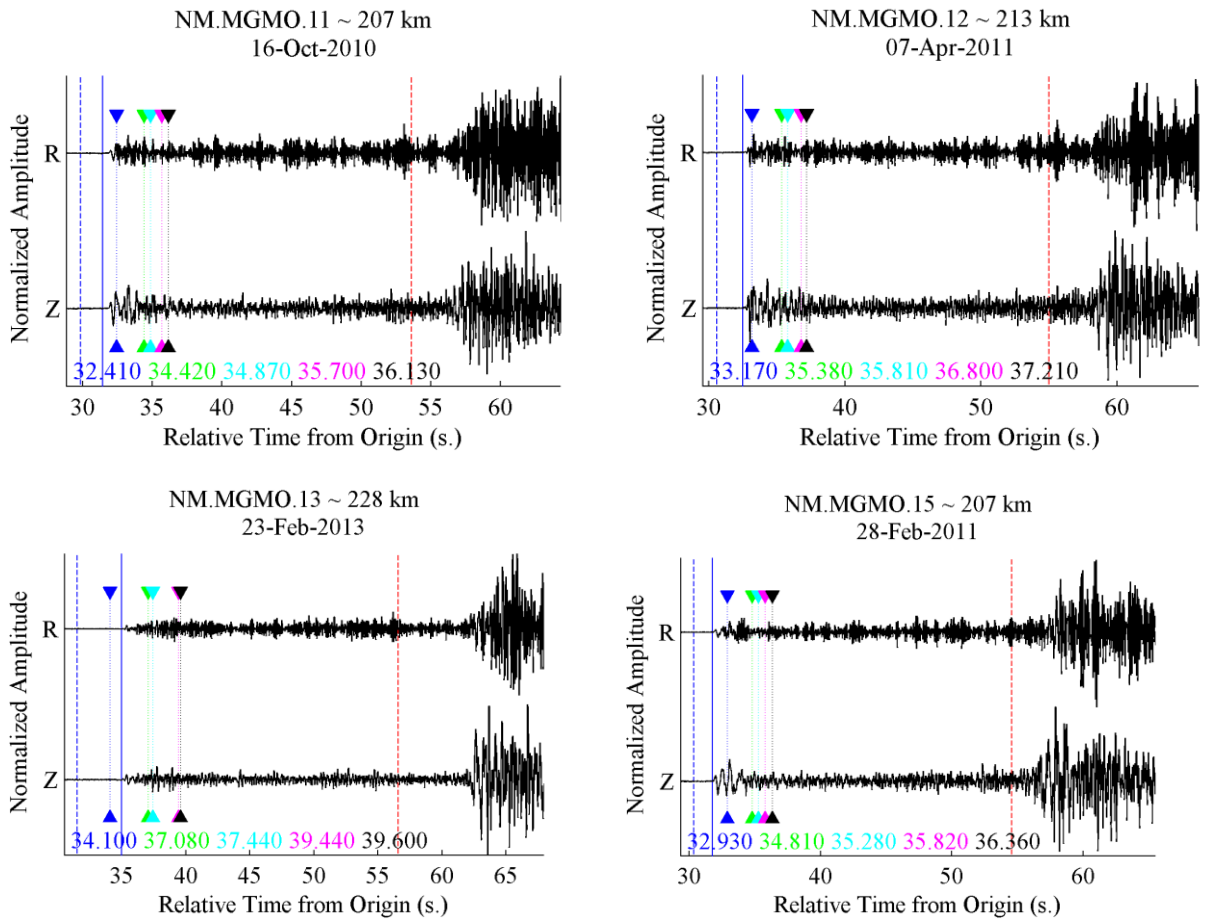

Figure 14. Continued.

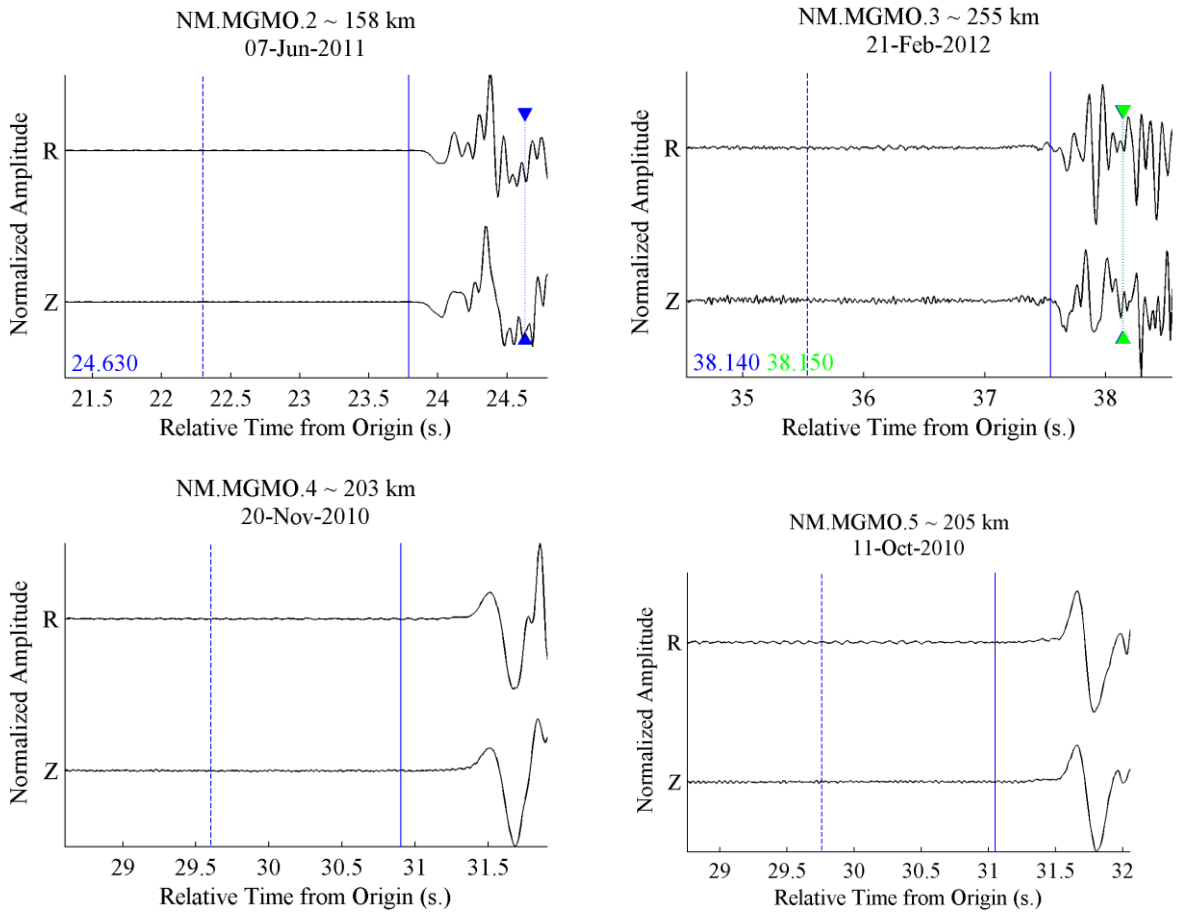

Figure 15. Recordings of 14 earthquakes at NM.MGMO station, showing the first P arrival and sorted based on descending order of SNR. This figure is similar to Figure 14. The initial P wave arrival time predicted by IRIS or the non-AR AIC picker is shown with dashed blue line, theoretical arrivals of various P phases predicted using Taup are shown with thin lines with triangles at both ends, and the final manual pick of the P wave arrival is shown with a solid blue line. Theoretical arrival time using the Ak135 earth model matches the observations well. The time series are normalized velocity records. The title of each plot depicts the name of the seismic network and station, epicentral distance, and earthquake date. Colored numbers are theoretical arrival times corresponding to the phase shown with the line of the same color and triangles at both ends.

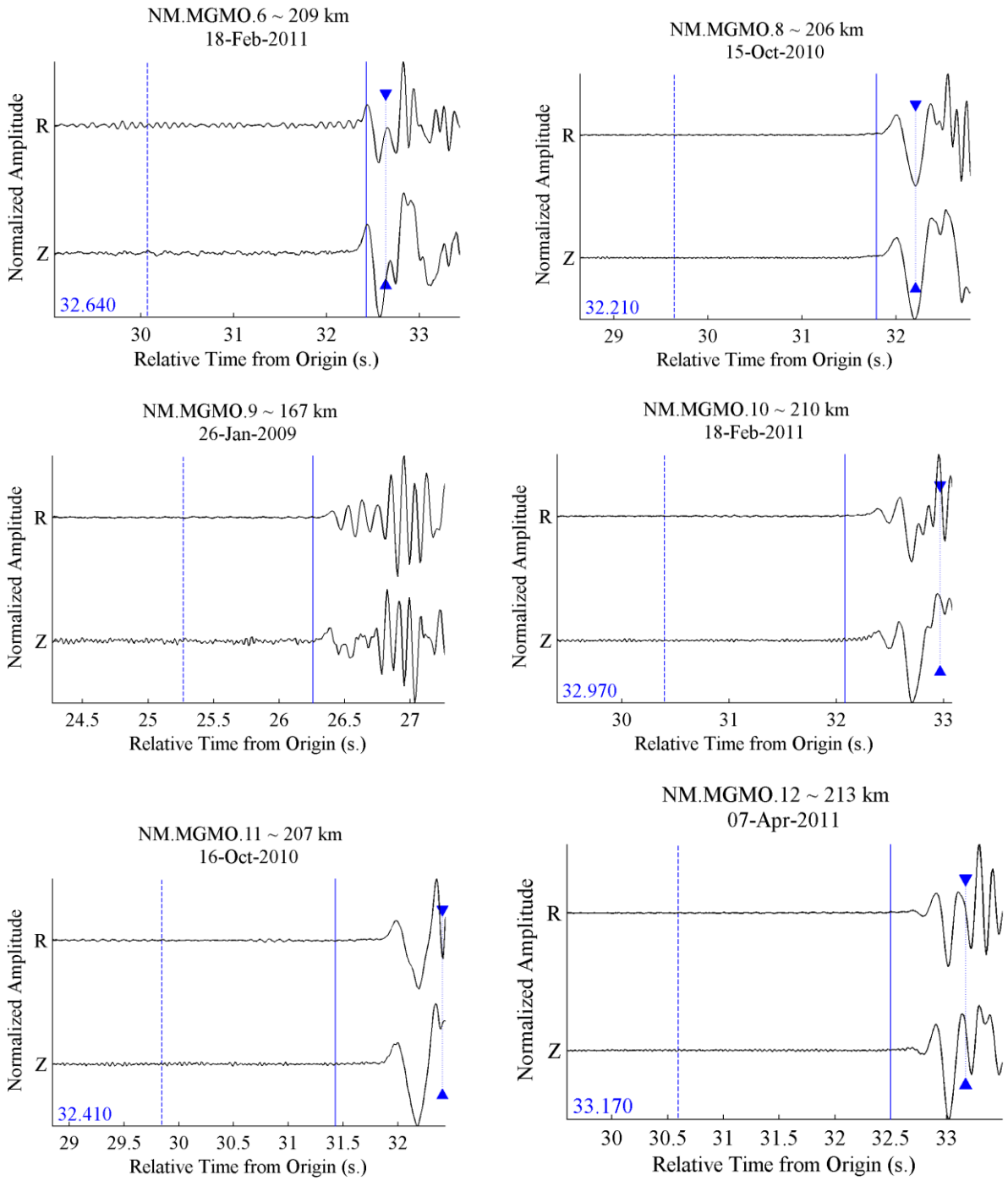

Figure 15. Continued.

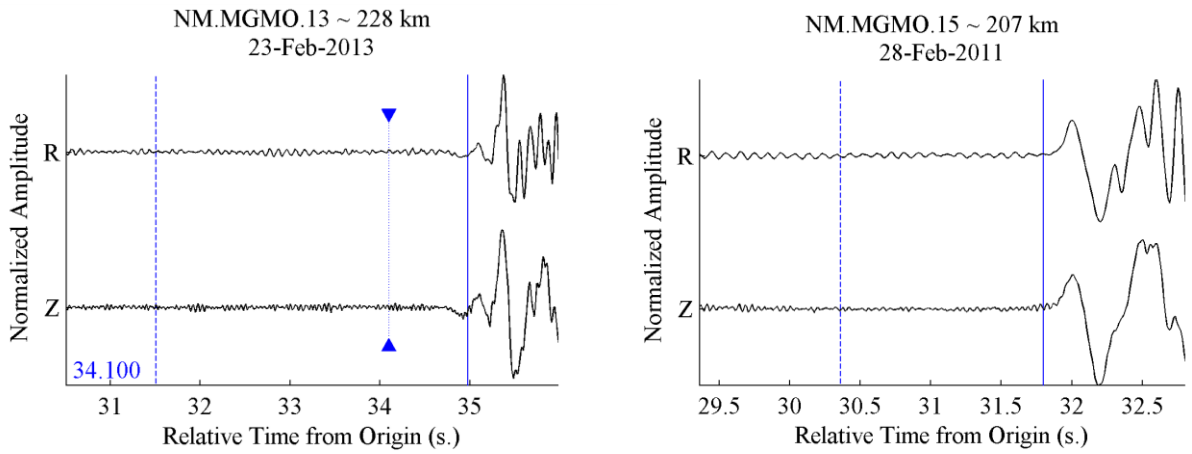

Figure 15. Continued.

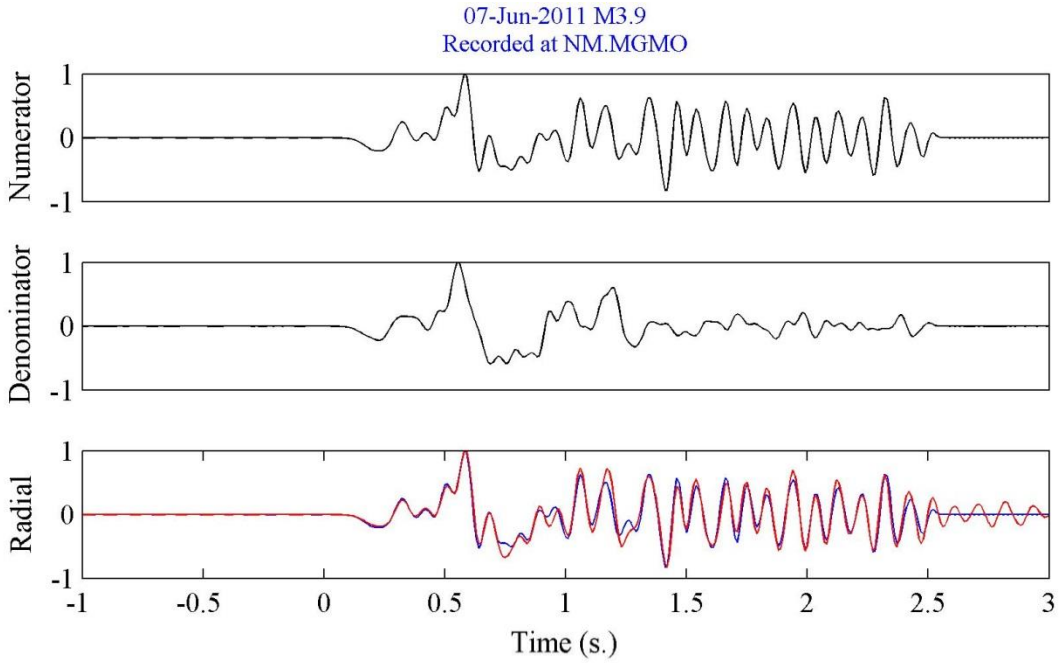

Figure 16. The deconvolution process is shown for the 7 June 2011 M3.9 earthquake where the denominator (vertical) is de-convolved from the numerator (radial) in the receiver function calculation process. The observed (blue) and predicted (red) radial components are very similar, showing a reliable deconvolution.

Synchronizing receiver functions prior to stacking

After the deconvolution of the vertical components from the radials, the receiver functions need to be slightly shifted in time to be synchronized with each other, because the manual arrival time pick might not be strictly consistent between different records.

We used a four-step process to perform synchronization:

(1) Removed those receiver functions that looked inconsistent with the majority of the receiver function pool for each station. We neglected those stations with less than three receiver functions to stack.
(2) Used cross-correlation to calculate the required time shift to align the initial portion of the receiver functions with that with highest SNR.
(3) Manually shifted the receiver functions that were not correctly synchronized with the one with the highest SNR in the previous step.
(4) Picked the length of receiver function to be matched with the theoretical one in the inversion process. Picking the receiver function length is performed by inspecting the overall similarity of RFs for the same station and avoiding the time beyond which the RFs start looking different from each other.

Figure 17 shows a sample for the stacking process for the station NM.MGMO where RFs are sorted with decreasing SNR. Grey dashed lines show the original RFs without synchronization and the thin black solid line shows the final position of the RFs after manual and automatic time shift. The vertical black line shows the time window used in the inversion process.

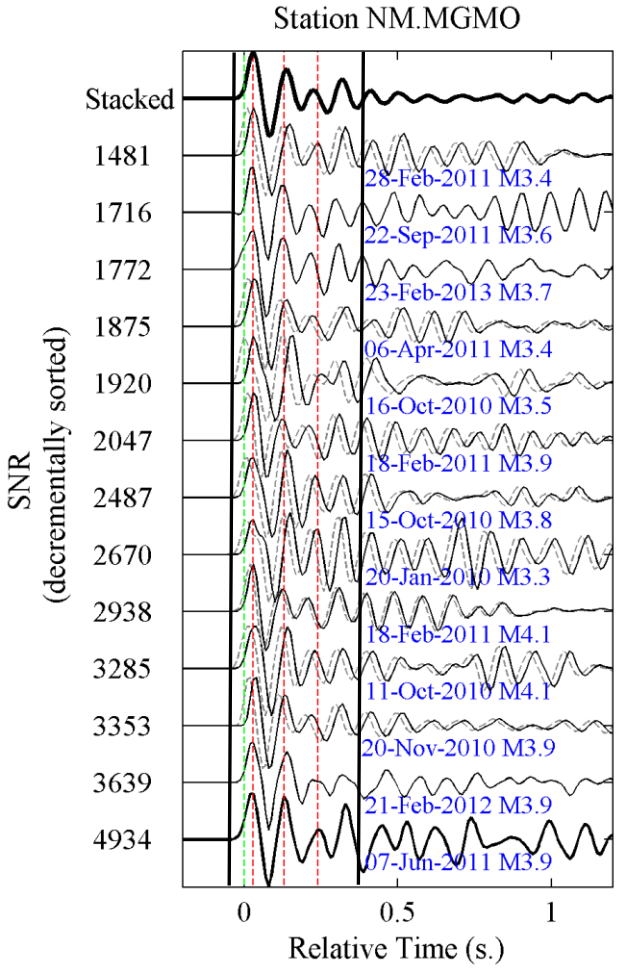

Figure 17. Recorded receiver functions for station MGMO are sorted vertically based on SNR. Relative time in the horizontal axis is from the onset of the P wave arrival. Vertical lines are used to guide synchronization of receiver functions with respect to the one with the highest SNR value. Time and magnitude of the earthquake is labelled beneath each receiver function. The stacked receiver function is plotted at the top.

Inversion of Receiver Functions for Shear Wave Velocity

In general, for a nonlinear inversion problem $\mathbf{G}(\mathbf{m}) = \mathbf{d}$, the solution can be obtained by using Occam's localized inversion technique (Aster et al., 2013) by means of the Jacobian matrix. Inversion is performed by minimizing the following objective function in a damped least-squares inversion (Aster et al., 2003):

$$F = \left\| \mathbf{J}(\mathbf{m})(\mathbf{m} + \Delta\mathbf{m}) - (\mathbf{d} - \mathbf{G}(\mathbf{m}) + \mathbf{J}(\mathbf{m})\mathbf{m} \right\|_2^2 + \lambda^2 \left\| \mathbf{L}(\mathbf{m} + \Delta\mathbf{m}) \right\|_2^2 \qquad (7)$$

where $\mathbf{m}$ is the unknown model parameters vector, $\Delta\mathbf{m}$ is the change in vector $\mathbf{m}$ with m elements, $\mathbf{d}$ is the observed data with n elements, $\mathbf{G}$ is a known n by m a matrix that relates model parameters with observations, $\mathbf{L}$ is the finite difference operator (Aster et al., 2013, Chapter 5) approximating the first or

second derivatives of the model parameters when it is multiplied by them and controls the smoothness of the solution, $\| \ \|_2^2$ is the L_2 norm squared, λ is the damping factor, and finally **J**(**m**) is the Jacobian matrix, presented by:

$$\mathbf{J}(\mathbf{m}) = \begin{bmatrix} \frac{\partial G_1(\mathbf{m})}{\partial m_1} & \cdots & \frac{\partial G_1(\mathbf{m})}{\partial m_m} \\ \vdots & \ddots & \vdots \\ \frac{\partial G_n(\mathbf{m})}{\partial m_1} & \cdots & \frac{\partial G_n(\mathbf{m})}{\partial m_1} \end{bmatrix}_{n \times m} \tag{8}$$

The Jacobian matrix holds the partial derivatives of the forward equation with respect to the model parameters. Selecting an appropriate damping factor λ is crucial for a successful inversion. Pujol (2007) gives good insight into the solution of nonlinear inverse problems using the Lenevberg-Marquardt method. Inversion for surface waves is performed iteratively using Occam's algorithm to find the model parameters (Aster et al., 2013):

$$\mathbf{m}^{k+1} = \left[\mathbf{J}(\mathbf{m}^k)^{\mathrm{T}} \mathbf{J}(\mathbf{m}^k) + \lambda^2 \mathbf{L}^{\mathrm{T}} \mathbf{L} \right]^{-1} \mathbf{J}(\mathbf{m}^k)^{\mathrm{T}} \left[\mathbf{d} - \mathbf{G}(\mathbf{m}^k) + \mathbf{J}(\mathbf{m}^k)\mathbf{m}^k \right] \tag{9}$$

where *k* is the iteration number, and the initial profile starts at $\mathbf{m}^0$. For the inversion we used a software package developed at the University of Saint Louis by Robert Herrmann. We used rftn96 for inversion and hrftn96 to generate synthetic receiver functions for an earth model.

Modification to Computer Programs in Seismology

The rftn96 source program was modified to keep the density fixed in the iteration process. Similar to Hosseini (2014), subroutine modls() from file modls.f were appropriately modified so the density parameter is set to the original value read from the model file instead calculating it from P wave velocity.

Initial Velocity Models for Inversion

The initial velocity model is important for a successful inversion. We assumed three layers over a half-space to model earth structure for receiver function inversion. The maximum depth that receiver function inversion can resolve is a function of shear-wave velocity (Ni et al. 2014) and therefore, an initial estimate of shear-wave velocity can help determine the depth of the velocity profile in the inversion process. We assumed various thicknesses for different layers for the depth profile of the earth model. In addition, the initial velocity structure of the earth model was varied as described in the following sections.

Depth Profile of the Earth Model

We used the data from our previous study (Ni and Somerville 2012) to estimate the maximum resolution depth. For each station we estimated the maximum depth as one tenth of the shear-wave velocity at that station (Ni et al. 2014). We used data from Ni et al. (2014) only at stations for which three or more earthquakes were used in the process of shear-wave velocity estimation. For each station, we then generated a suite of three-layer earth models in which the summation of thicknesses of all three layers are almost equal to that estimated from average shear-wave velocity profile obtained from Ni et al. (2014). In

this process, we considered all possible combinations of layer thicknesses conditioned on layer thickness increasing with depth. The thickness for layer #1 closest to surface ranges from 1 to 31 every 3 meters, for layer #2 ranges from 10 to 115 every 10 meters and for layer #3 ranges from 20 to 190 every 20 meters. From all of the combinations with various thicknesses for each layer, we matched the best 15 having minimum error in their overall depth and maximum penetration depth for each station. Table 2 provides an example of various depth combinations for the earth model for station TA.V40A.

Table 2. Various combinations for layers' thickness at TA.V40A station

Average VS (m/s)	Layer #1 Thickness (m)	Layer #2 Thickness (m)	Layer #3 Thickness (m)	Earth Model Depth (m)
1422	1	20	120	141
	1	60	80	141
	25	40	80	145
	19	40	80	139
	7	20	120	147
	7	60	80	147
	13	40	80	133
	13	20	120	153
	13	60	80	153

Velocity Structure of the Earth Model

For each velocity model at each station, we further assigned seven sets of initial shear-wave velocity profiles. The combination of seven sets of shear-wave velocity profiles increases the chance of obtaining a realistic V_S velocity model in the inversion. These seven sets are provided in Table 3.

Table 3. Seven sets of background shear wave velocities for the starting model used in the inversion

Parameter Name	Layer #1	Layer #2	Layer #3	Half-Space
Low Velocity (km/s)	0.05	0.10	0.10	0.11
Linearly Increasing from low to medium velocity (km/s)	0.10	0.20	0.50	0.80
Medium velocity (km/s)	0.80	0.80	0.80	0.85
Linearly Increasing from medium to high velocity (km/s)	0.80	1.50	2.20	2.50
High Velocity (km/s)	2.20	2.20	2.20	2.50
Average Velocity (km/s)	$V_{S,ave}$	$V_{S,ave}$	$V_{S,ave}$	1.1 $V_{S,ave}$
Linearly Increasing based on Average Velocity (km/s)	0.75$V_{S,ave}$	$V_{S,ave}$	1.25 $V_{S,ave}$	1.35 $V_{S,ave}$
Density (g/cc)	1.80	1.85	1.85	1.90
V_P/V_S ratio	1.80	1.80	1.80	1.90

* $V_{S,ave}$ is the average shear-wave velocity from Ni and Somerville (2013)

Final Velocity Models

We obtained the final velocity model by comparing the best match between theoretical and observed receiver functions at each station. Match quality is expressed as percent of Signal Power Fit (SPF). Inversion at each station for various earth models yielded multiple inverted shear-wave velocity profiles. Table 4 shows the number of various earth models used in the inversion process for each station. A total of ~46,000 inversions were performed in this study.

For each of the many shear-wave velocity profiles at each station, we calculated three parameters:

(1) Time-averaged shear-wave velocity over the total depth of the profile ($V_{S,T\text{-}Ave}$)

(2) Arithmetic average shear-wave velocity over the total depth of the profile ($V_{S,\,Ave}$)

(3) Time-averaged shear-wave velocity for upper 30 meters (V_{S30})

For each station, we sorted inverted velocity models with respect to SPF and calculated the final values for three parameters $V_{S,T\text{-}Ave}$, $V_{S,Ave}$, and V_{S30} by averaging corresponding values from earth models that have a minimum threshold SPF error with the highest SPF. Threshold error was selected to be 15 percent in this study.

Figure 18 shows the inverted earth model, along with the predicted and observed receiver functions at NM.MGMO station. We intentionally did not remove any station because of low SPF as this value is relative between stations due to various lengths of the receiver function used in inversion, and the initial velocity model. In addition, there are parameters such as inversion time-window length that can be modified to get slightly modified results and improve the shear wave velocity at stations that have low SPF value. For recordings with low SPF, shorter time-window lengths can be used to attain an improved (higher SPF) inversion. This fact can be observed in our inversion in Figure 19 where SPF has decreasing trend with inversion time-window length. Future studies can pick an appropriate time-window lengths for those stations that currently have low SPF. We also looked at the trend of SPF with average SNR as shown in Figure 20 and did not find a trend, which shows that quality of inversion is not affected by the SNR of the recordings as expected.

Inverted velocity profiles and the match between the observed and predicted receiver functions for all stations are provided in Appendix A. Appendix A provides the plots for radial and vertical components of recordings with highest SNR and appropriate-looking waveforms for each station. Also provided in Appendix A are the receiver functions along with the stacked RF used in the inversion along with the match between observed and predicted RFs in the inversion process. Finally, some of the inverted velocity models with highest SPF are provided in a table incrementally sorted for SPF. In the next section shear-wave velocities obtained at CEUS stations are presented on maps and in a table.

Table 4. Number of receiver function inversions performed in this study.

*	Station	Inv. V_S	*	Station	Inv. V_S	*	Station	Inv. V_S	*	Station	Inv. V_S
1	CPCT	**105**	141	E52A	**112**	281	R58B	**112**	421	V52A	**112**
2	FPAL	**112**	142	E53A	**112**	282	S21A	**112**	422	V53A	**112**
3	SWET	**56**	143	E54A	**112**	283	S22A	**112**	423	V54A	**91**
4	UOM1	**112**	144	F51A	**112**	284	S23A	**7**	424	W23A	**49**
5	UOM2	**112**	145	F52A	**112**	285	S24A	**112**	425	W24A	**112**
6	UOM3	**112**	146	F55A	**112**	286	S25A	**112**	426	W25A	**112**
7	UOM4	**112**	147	G53A	**112**	287	S26A	**112**	427	W26A	**112**
8	TKL	**112**	148	G55A	**112**	288	S27A	**112**	428	W27A	**112**
9	TX31	**112**	149	G57A	**112**	289	S28A	**112**	429	W29A	**112**
10	CCM	**112**	150	H25A	**112**	290	S31A	**112**	430	W30A	**35**
11	SSPA	**112**	151	H55A	**21**	291	S32A	**7**	431	W31A	**35**
12	WCI	**112**	152	H56A	**112**	292	S33A	**35**	432	W32A	**7**
13	WVT	**112**	153	H58A	**112**	293	S34A	**112**	433	W33A	**35**
14	ACCN	**112**	154	I27A	**112**	294	S35A	**112**	434	W34A	**112**
15	BMNY	**112**	155	I28A	**7**	295	S36A	**35**	435	W35A	**105**
16	BRNY	**112**	156	I55A	**21**	296	S38A	**63**	436	W36A	**112**
17	FLET	**112**	157	J27A	**112**	297	S39A	**56**	437	W37A	**112**
18	FRNY	**112**	158	J28A	**21**	298	S40A	**98**	438	W37B	**112**
19	HBVT	**112**	159	J30A	**112**	299	S41A	**112**	439	W38A	**112**
20	HCNY	**112**	160	J31A	**14**	300	S42A	**98**	440	W39A	**112**
21	KSPA	**112**	161	K22A	**112**	301	S44A	**112**	441	W40A	**112**
22	LUPA	**112**	162	K30A	**21**	302	S45A	**112**	442	W41A	**112**
23	MCVT	**112**	163	K31A	**7**	303	S46A	**35**	443	W41B	**63**
24	MMNY	**112**	164	K43A	**112**	304	S47A	**112**	444	W42A	**42**
25	MSNJ	**112**	165	KMSC	**112**	305	S48A	**112**	445	W45A	**7**
26	MVL	**112**	166	KSCO	**84**	306	S49A	**112**	446	W46A	**35**
27	NCB	**112**	167	L29A	**21**	307	S50A	**70**	447	W47A	**77**
28	NPNY	**112**	168	L30A	**112**	308	S51A	**112**	448	W48A	**112**
29	ODNJ	**112**	169	L31A	**112**	309	S52A	**112**	449	W49A	**112**
30	PAL	**112**	170	L44A	**112**	310	S53A	**112**	450	W50A	**56**
31	PANJ	**112**	171	L53A	**112**	311	S54A	**112**	451	W51A	**14**
32	POTS	**112**	172	M31A	**112**	312	S55A	**112**	452	W52A	**112**
33	PTN	**112**	173	M44A	**112**	313	S57A	**112**	453	W53A	**7**
34	WCNY	**112**	174	M52A	**112**	314	S58A	**112**	454	W54A	**56**
35	WVNY	**112**	175	M54A	**56**	315	SFIN	**112**	455	WHTX	**112**
36	BLO	**112**	176	MSTX	**7**	316	T22A	**84**	456	X23A	**28**
37	CGM3	**112**	177	N23A	**84**	317	T23A	**112**	457	X24A	**112**
38	CLTN	**112**	178	N31A	**21**	318	T24A	**112**	458	X25A	**35**
39	FVM	**112**	179	N32A	**112**	319	T24B	**112**	459	X26A	**112**
40	GLAT	**35**	180	N44A	**112**	320	T25A	**112**	460	X27A	**112**
41	GNAR	**112**	181	N45A	**112**	321	T26A	**112**	461	X28A	**112**

42	HALT	**112**	182	N46A	**112**	322	T27A	**112**	462	X29A	**35**
43	HBAR	**112**	183	N50A	**112**	323	T28A	**35**	463	X30A	**35**
44	HENM	**49**	184	N51A	**112**	324	T29A	**35**	464	X31A	**70**
45	HICK	**49**	185	N52A	**112**	325	T30A	**35**	465	X32A	**112**
46	LNXT	**35**	186	N53A	**56**	326	T31A	**21**	466	X33A	**63**
47	LPAR	**112**	187	N54A	**112**	327	T32A	**7**	467	X34A	**21**
48	MGMO	**112**	188	N55A	**112**	328	T33A	**35**	468	X35A	**63**
49	OLIL	**84**	189	O27A	**112**	329	T34A	**49**	469	X36A	**56**
50	PARM	**35**	190	O28A	**112**	330	T35A	**84**	470	X37A	**56**
51	PBMO	**112**	191	O29A	**14**	331	T36A	**42**	471	X38A	**35**
52	PEBM	**35**	192	O30A	**7**	332	T37A	**28**	472	X39A	**77**
53	PENM	**35**	193	O31A	**112**	333	T38A	**112**	473	X40A	**112**
54	PLAL	**70**	194	O32A	**112**	334	T39A	**35**	474	X41A	**70**
55	PVMO	**35**	195	O43A	**112**	335	T40A	**112**	475	X42A	**77**
56	SIUC	**112**	196	O44A	**28**	336	T41A	**105**	476	X43A	**35**
57	SLM	**112**	197	O47A	**21**	337	T42A	**35**	477	X44A	**7**
58	UALR	**112**	198	O49A	**91**	338	T43A	**112**	478	X46A	**112**
59	USIN	**56**	199	O50A	**112**	339	T44A	**77**	479	X47A	**28**
60	X102	**112**	200	O51A	**112**	340	T45A	**49**	480	X48A	**28**
61	X201	**112**	201	O52A	**112**	341	T46A	**112**	481	X49A	**112**
62	X301	**112**	202	O53A	**112**	342	T47A	**112**	482	X50B	**112**
63	121A	**0**	203	O54A	**112**	343	T48A	**91**	483	X51A	**112**
64	123A	**21**	204	O55A	**112**	344	T49A	**42**	484	X52A	**105**
65	124A	**35**	205	O56A	**112**	345	T50A	**112**	485	X53A	**112**
66	125A	**21**	206	P23A	**112**	346	T51A	**112**	486	X54A	**112**
67	126A	**35**	207	P24A	**28**	347	T52A	**91**	487	X56A	**112**
68	127A	**21**	208	P25A	**28**	348	T53A	**112**	488	Y22D	**112**
69	128A	**21**	209	P27A	**28**	349	T54A	**112**	489	Y23A	**7**
70	129A	**91**	210	P29A	**112**	350	T55A	**63**	490	Y24A	**84**
71	130A	**91**	211	P30A	**112**	351	T56A	**63**	491	Y25A	**84**
72	131A	**84**	212	P31A	**112**	352	T57A	**91**	492	Y26A	**84**
73	133A	**84**	213	P32A	**112**	353	T58A	**91**	493	Y27A	**84**
74	134A	**112**	214	P38A	**112**	354	TASO	**91**	494	Y28A	**84**
75	135A	**28**	215	P40A	**112**	355	TUL1	**112**	495	Y29A	**84**
76	136A	**49**	216	P41A	**112**	356	U21A	**28**	496	Y30A	**84**
77	137A	**35**	217	P42A	**112**	357	U22A	**112**	497	Y32A	**77**
78	140A	**14**	218	P43A	**91**	358	U23A	**112**	498	Y33A	**56**
79	143A	**21**	219	P44A	**112**	359	U24A	**112**	499	Y34A	**49**
80	151A	**112**	220	P45A	**14**	360	U25A	**112**	500	Y35A	**35**
81	152A	**112**	221	P46A	**91**	361	U26A	**35**	501	Y36A	**35**
82	153A	**112**	222	P47A	**49**	362	U27A	**35**	502	Y37A	**42**
83	154A	**112**	223	P50A	**112**	363	U28A	**112**	503	Y38A	**7**
84	155A	**112**	224	P51A	**112**	364	U31A	**112**	504	Y39A	**112**
85	221A	**112**	225	P52A	**91**	365	U32A	**21**	505	Y40A	**7**

86	224A	**7**	226	P53A	**84**	366	U33A	**14**	506	Y41A	**112**
87	225A	**21**	227	P54A	**49**	367	U34A	**63**	507	Y42A	**7**
88	226B	**21**	228	P55A	**112**	368	U35A	**28**	508	Y43A	**35**
89	227A	**21**	229	P56A	**77**	369	U36A	**56**	509	Y46A	**112**
90	228A	**91**	230	Q22A	**77**	370	U37A	**112**	510	Y47A	**28**
91	229A	**91**	231	Q23A	**112**	371	U38A	**112**	511	Y48A	**112**
92	230A	**35**	232	Q24A	**112**	372	U39A	**112**	512	Y49A	**112**
93	231A	**35**	233	Q25A	**112**	373	U40A	**112**	513	Y50A	**112**
94	232A	**21**	234	Q26A	**112**	374	U41A	**77**	514	Y51A	**112**
95	233A	**14**	235	Q29A	**7**	375	U42A	**7**	515	Y52A	**112**
96	234A	**21**	236	Q31A	**112**	376	U43A	**112**	516	Y53A	**112**
97	236A	**49**	237	Q32A	**112**	377	U44A	**35**	517	Y54A	**63**
98	237A	**84**	238	Q39A	**112**	378	U44B	**7**	518	Y55A	**35**
99	240A	**112**	239	Q40A	**112**	379	U45A	**35**	519	Z22A	**91**
100	241A	**112**	240	Q41A	**112**	380	U46A	**7**	520	Z24A	**112**
101	248A	**7**	241	Q42A	**112**	381	U47A	**7**	521	Z25A	**112**
102	324A	**7**	242	Q43A	**112**	382	U48A	**21**	522	Z26A	**112**
103	325A	**35**	243	Q44A	**112**	383	U49A	**21**	523	Z27A	**112**
104	326A	**35**	244	Q45A	**28**	384	U50A	**28**	524	Z28A	**112**
105	329A	**49**	245	Q46A	**77**	385	U51A	**112**	525	Z29A	**112**
106	330A	**112**	246	Q47A	**21**	386	U52A	**7**	526	Z30A	**112**
107	331A	**112**	247	Q49A	**112**	387	U53A	**84**	527	Z31A	**77**
108	332A	**112**	248	Q50A	**112**	388	U54A	**112**	528	Z32A	**63**
109	333A	**14**	249	Q51A	**63**	389	U55A	**112**	529	Z33A	**98**
110	334A	**112**	250	Q52A	**112**	390	U56A	**105**	530	Z34A	**21**
111	335A	**112**	251	Q53A	**98**	391	V21A	**105**	531	Z35A	**21**
112	336A	**112**	252	Q54A	**35**	392	V22A	**112**	532	Z36A	**14**
113	341A	**84**	253	Q55A	**35**	393	V23A	**112**	533	Z37A	**35**
114	425A	**112**	254	Q57A	**35**	394	V24A	**7**	534	Z39A	**112**
115	426A	**112**	255	R21A	**77**	395	V25A	**112**	535	Z40A	**49**
116	428A	**112**	256	R22A	**7**	396	V26A	**35**	536	Z41A	**7**
117	429A	**84**	257	R23A	**112**	397	V27A	**35**	537	Z42A	**35**
118	430A	**112**	258	R24A	**112**	398	V28A	**35**	538	Z48A	**7**
119	431A	**112**	259	R25A	**112**	399	V30A	**112**	539	Z49A	**112**
120	432A	**112**	260	R26A	**112**	400	V31A	**112**	540	Z50A	**112**
121	433A	**112**	261	R27A	**112**	401	V32A	**98**	541	Z51A	**112**
122	434A	**112**	262	R38A	**112**	402	V33A	**42**	542	Z52A	**112**
123	435B	**112**	263	R39A	**112**	403	V34A	**28**	543	Z53A	**28**
124	526A	**112**	264	R40A	**56**	404	V35A	**42**	544	Z54A	**42**
125	527A	**112**	265	R41A	**112**	405	V36A	**21**	545	Z55A	**42**
126	532A	**112**	266	R42A	**112**	406	V37A	**105**	546	Z57A	**42**
127	534A	**112**	267	R43A	**98**	407	V38A	**112**	547	ACSO	**91**
128	632A	**70**	268	R44A	**112**	408	V39A	**49**	548	AMTX	**112**
129	735A	**91**	269	R45A	**7**	409	V40A	**112**	549	BINY	**91**

130	833A	**35**	270	R46A	**49**	410	V41A	**70**	550	BLA	**112**
131	835A	**70**	271	R47A	**112**	411	V42A	**112**	551	CBN	**112**
132	934A	**105**	272	R48A	**112**	412	V43A	**112**	552	JCT	**7**
133	ABTX	**28**	273	R49A	**112**	413	V44A	**7**	553	LONY	**112**
134	BGNE	**56**	274	R50A	**56**	414	V45A	**7**	554	LRAL	**112**
135	D51A	**7**	275	R51A	**21**	415	V46A	**7**	555	MIAR	**112**
136	D52A	**112**	276	R52A	**112**	416	V47A	**112**	556	MNTX	**112**
137	D53A	**112**	277	R53A	**112**	417	V48A	**112**	557	NCB	**28**
138	D54A	**112**	278	R54A	**112**	418	V49A	**112**	558	OXF	**112**
139	D55A	**112**	279	R55A	**112**	419	V50A	**35**	559	SDCO	**7**
140	D56A	**112**	280	R57A	**112**	420	V51A	**105**	560	TZTN	**112**

* Number of station and seismic network color code based on the following color map:

ET	IM	IU	LD	NM	TA	US

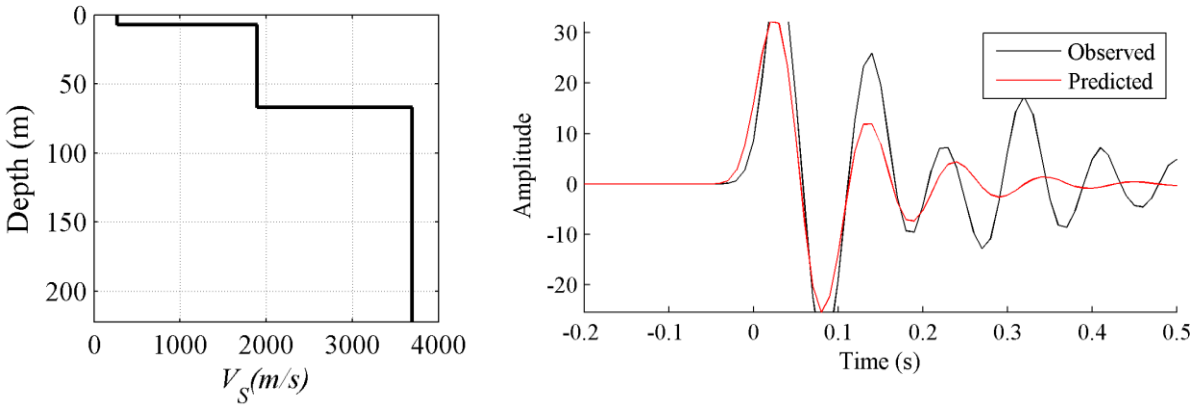

Figure 18. (left) Velocity structure with best SPF ratio acquired from inversion of receiver function. (right) Match between predicted (red) and observed (black) receiver functions at NM.MGMO seismic station.

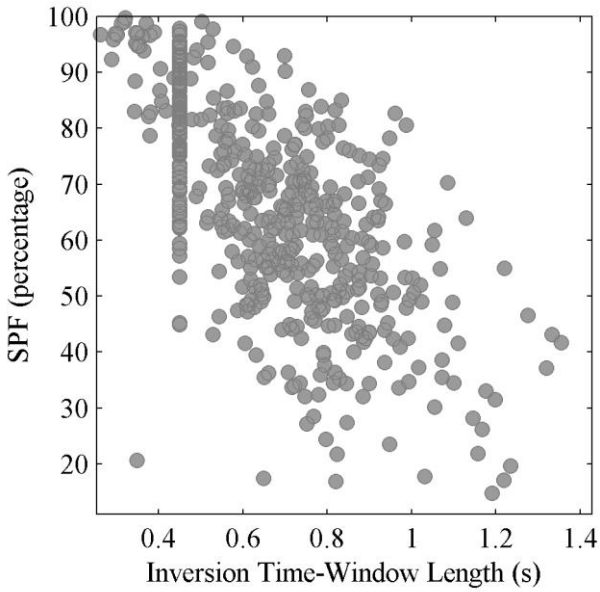

Figure 19. The correlation between inversion window length and quality of inversion (SPF).

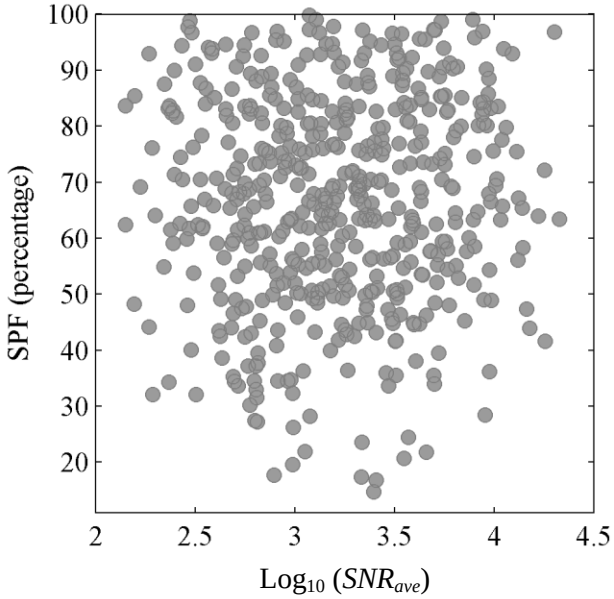

Figure 20. The correlation between logarithmic SNR values and inversion quality parameter (SPF).There is no obvious trend in the data.

Shallow Shear Wave Velocity Across the Central and Eastern United States

This section provides maps of three velocity parameters $V_{S,T\text{-}Ave}$, $V_{S,Ave}$, and V_{S30} in the Central and Eastern United States and its comparison with average shallow shear-wave velocity estimated by Ni and Somerville (2013). Figure 21 shows the time-averaged shear wave velocities for the overall depth of the inverted velocity models ($V_{S,T\text{-}Ave}$) which can be compared with those from Ni and Somerville (2013) in Figure 22. A comparison with Ni and Somerville (2013) shows a similar trend.

We compared the consistency of our results with the geological setting. The American Great Plains were covered by the Western Interior Seaway during the Cretaceous, which left sedimentary deposits. The thickness of the sediments reaches to 1 or 2 km and they are expected to have relatively lower velocities. In the Midwest region, ancient Paleozoic sedimentary rock exists having relatively high-velocity at shallow depth beneath residual soils (Conn, 2013). Figure 23 shows the approximate boundaries of these geological regions.

Our results are consistent with the geology of the Central and Eastern United States. The shear-wave velocities that we obtained are systematically lower in the Mississippi Embayment and Great Plains. In contrast, the Western and Eastern margins of the Mid West region possess higher velocities than most of the CEUS. This is reflected in the map of V_{S30} based on topographic slope shown in Figure 24. In our results, the low velocity region of the Mississippi Embayment extends further north than expected. The same trend in the overall distribution of the velocities is observed in Ni and Somerville (2013).

Our estimates of V_{S30} and compared with those of the USGS map in Figure 25. The USGS map was based on correlation of topographic slope with the NEHRP site categories, but site classes A ($V_{S30} > 1{,}500$ m/s) and B (760 m/s $< V_{S30} <$ 1,500 m/s) were grouped together, so their site class B is for $V_{S30} >$ 760 m/s. Site class A was ignored for two reasons. First, there was very little V_{S30} data greater than 760 m/s with which to calibrate the model. Second, once in hard rock, the slope may have little bearing on V_{S30}, and in the CEUS, very hard (fast) units may have low slope. This resulted in the inability to resolve the V_{S30} of the high velocity regions of the CEUS using slope.

Most of the estimated shear-wave velocities in this study are ~30 percent lower than those of Ni and Somerville (2013) as presented in Figure 26. The difference may be in the methodology used in this study compared to the technique of Ni and Somerville (2012). In this study we assumed that the water table is lower than the structure being imaged, which affects the Poisson's ratio and consequently V_P/V_S ratio used in the inversion model. We also compare our results with measured values reported by Kim et al. (2016) presented in Table 5 and Figure 27. These results are in reasonably close agreement.

Table 5. Comparison of V_{S30} values in this study with Kim et al. (2016).

Station Name	V_{S30} (m/s)	
	This Study	Kim et al. (2016)
NM.LNXT	270*	250
NM.OLIL	453	475
NM.UALR	1038	1288
NM.USIN	750	705
US.LONY	1996	1425
US.NCB	1819	1503
US.WMOK	1927	1859

* based on the frequency of V_{S30} values, data points greater than 500 m/s were excluded:

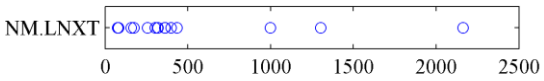

Values for $V_{S,Ave}$, and V_{S30} in the Eastern Central United States are shown in Figures 28 and 29, and Figure 30 shows the average station SNR based on participating receiver functions. Data used in these figures are given in Table 6, which summarizes the results presented in the maps.

Current Scope and Future Enhancements

In this study a large number of earthquake records in the CEUS seismic were collected and analyzed. The development of a high frequency receiver function database in the CEUS is one of the important outcomes of this study. In the data processing, factors negatively affecting the reliability of the representative receiver function at CEUS station were constrained using approaches described in the report.

We inverted the receiver functions to obtain layered velocity model at CEUS stations using a resource-intensive technique that varied velocity and depth background models for the starting earth structure. Such inversion technique maximizes spanning of the solution space; however there are still parameters that can be improved such as the V_P/V_S which require input from ground water level at CEUS stations. In addition, receiver function inversion itself may suffer from non-uniqueness that affects the absolute thickness of layers in the imaged profile as described earlier. Therefore, the database of receiver functions along with the SNR data can be used to identify stations for which the receiver function database can be improved or finding the station for which the receiver functions are already satisfactory and inversion requires improvement.

We share the outcome and routines used in this study with the scientific community to foster further progress in characterizing the near-surface seismic wave velocity characteristics in the CEUS.

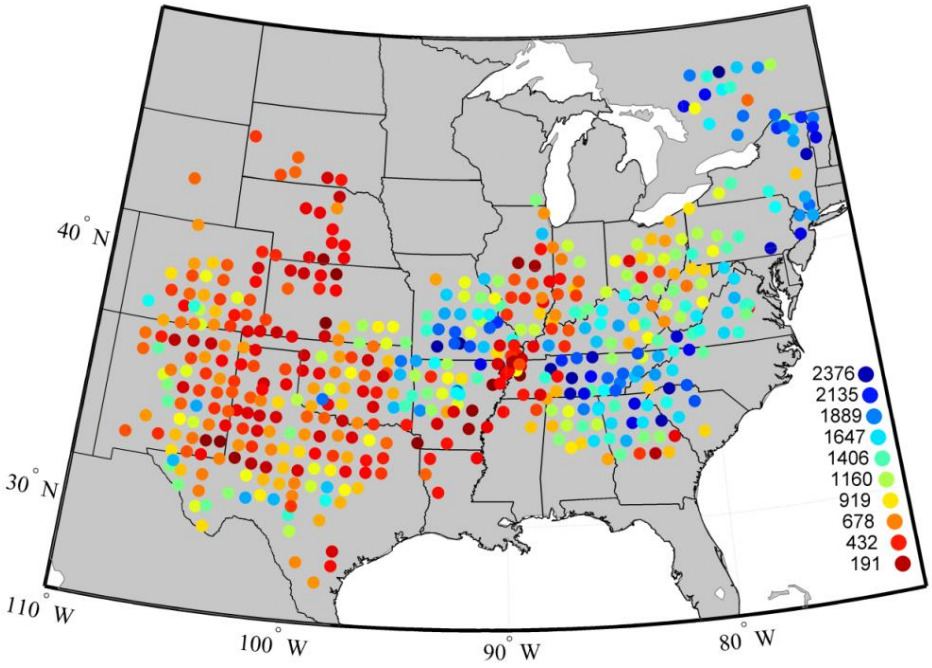

Figure 21. Time-averaged shear wave velocities $V_{S,T\text{-}Ave}$ (m/s) across the CEUS.

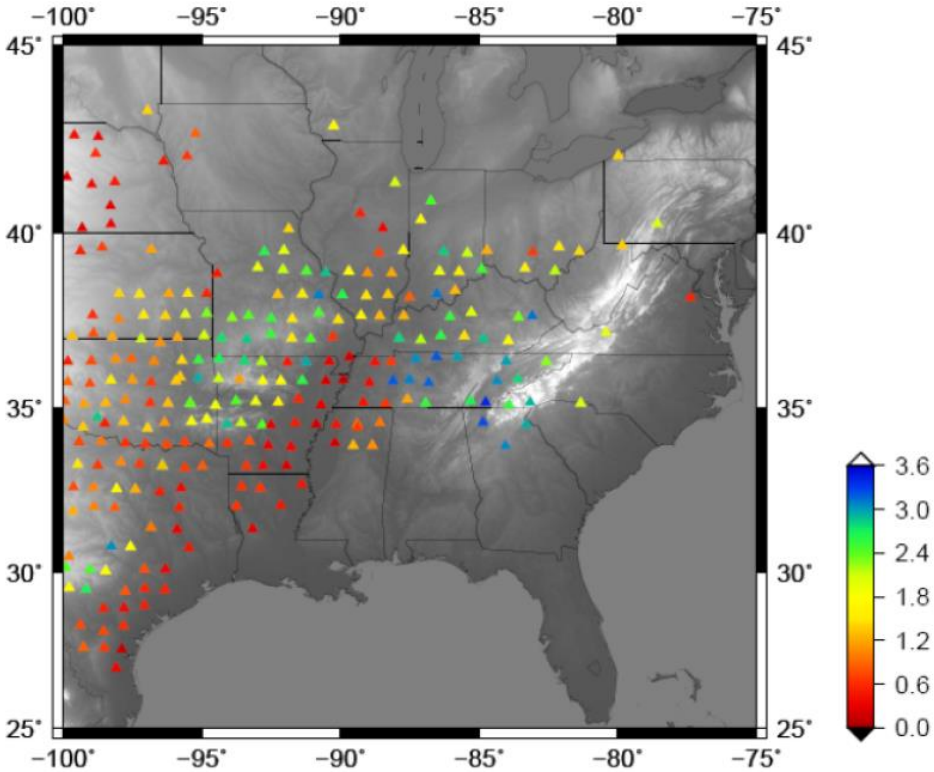

Figure 22. Average shear-wave velocities in the CEUS from Ni and Somerville (2013) measured with correlation time window of 0.3 sec and highpass frequency of 1Hz. Units are in km/s.

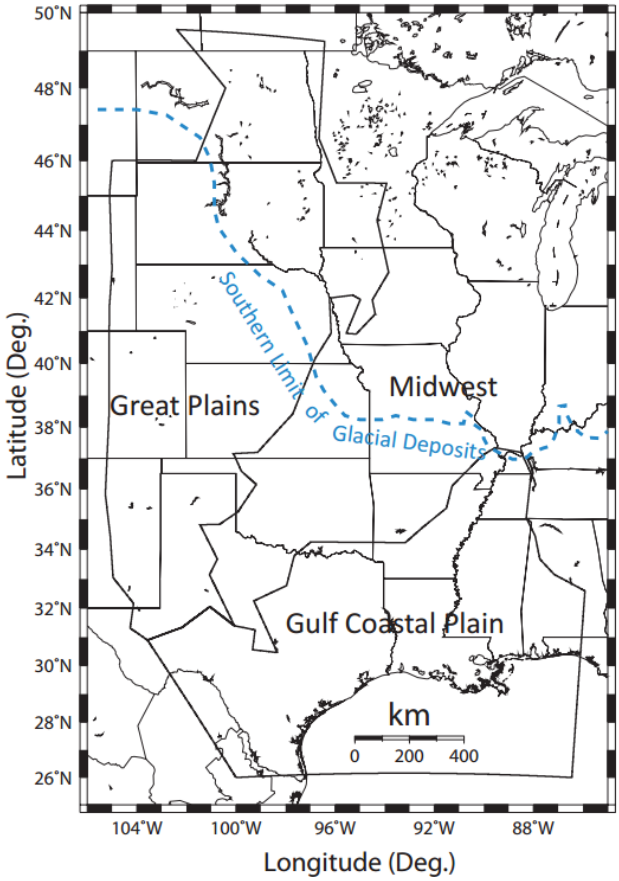

Figure 23. Geologic boundaries for regionalization of the Central U.S. The southern limit of glacial deposits is in blue. Source: Conn (2013).

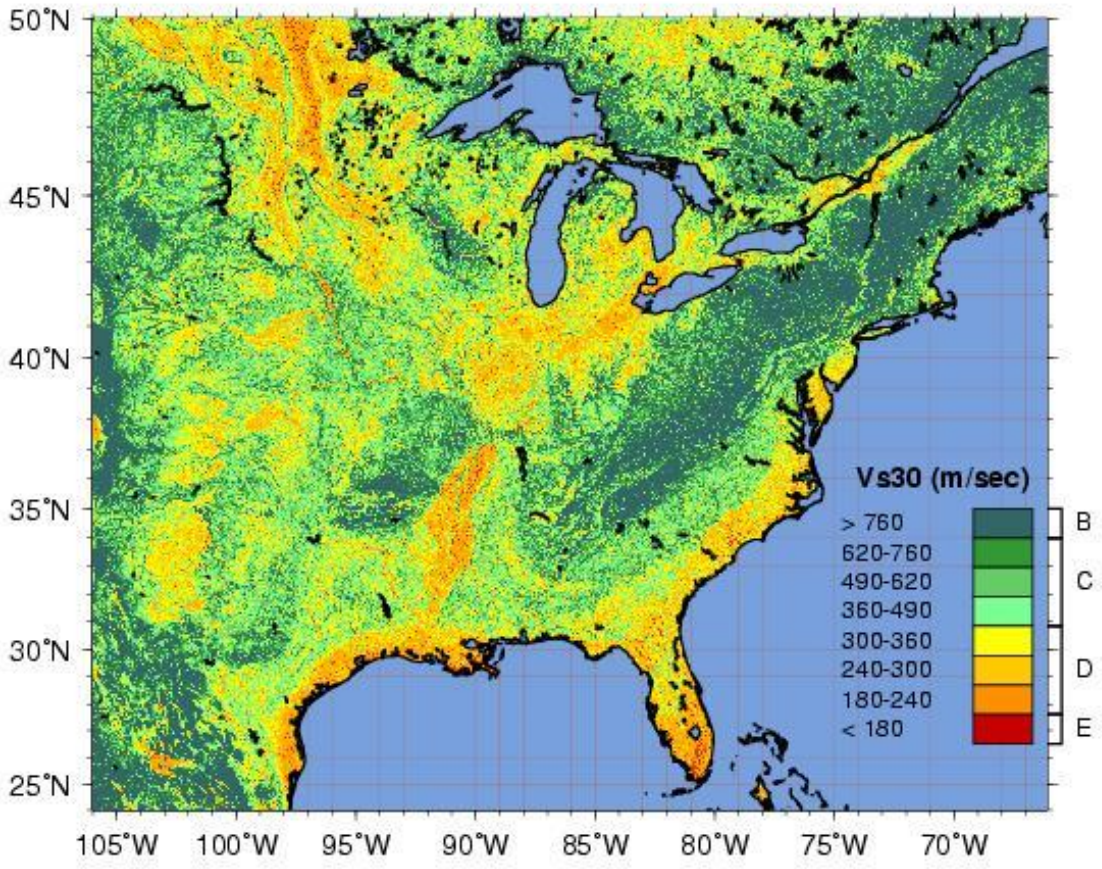

Figure 24. V_{S30} from topographic slope. Source: USGS.
http://earthquake.usgs.gov/hazards/apps/vs30/predefined.php

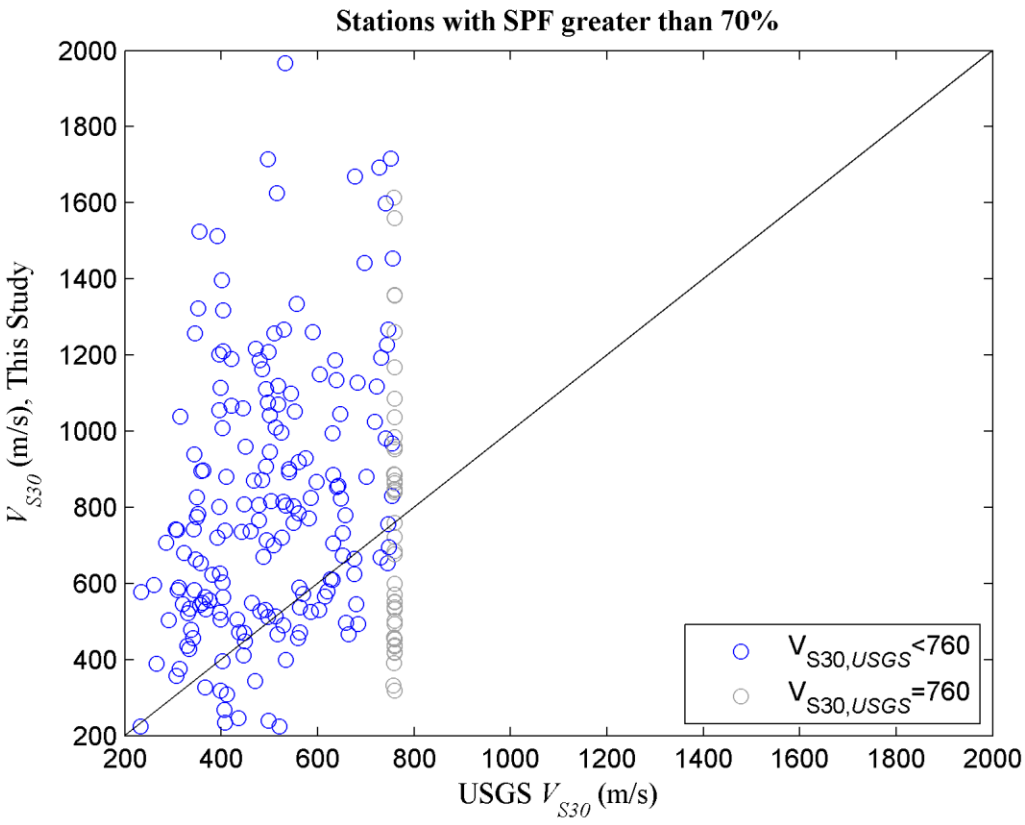

Figure 25. V_{S30} values from this study are plotted against those from USGS at the stations with SPF greater than 70 percent. The USGS values are limited to 760 m/s. The orthogonal line in the plot has a 45 degree angle and passes through the origin. The USGS V_{S30} values across CEUS are plotted in Figure 24.

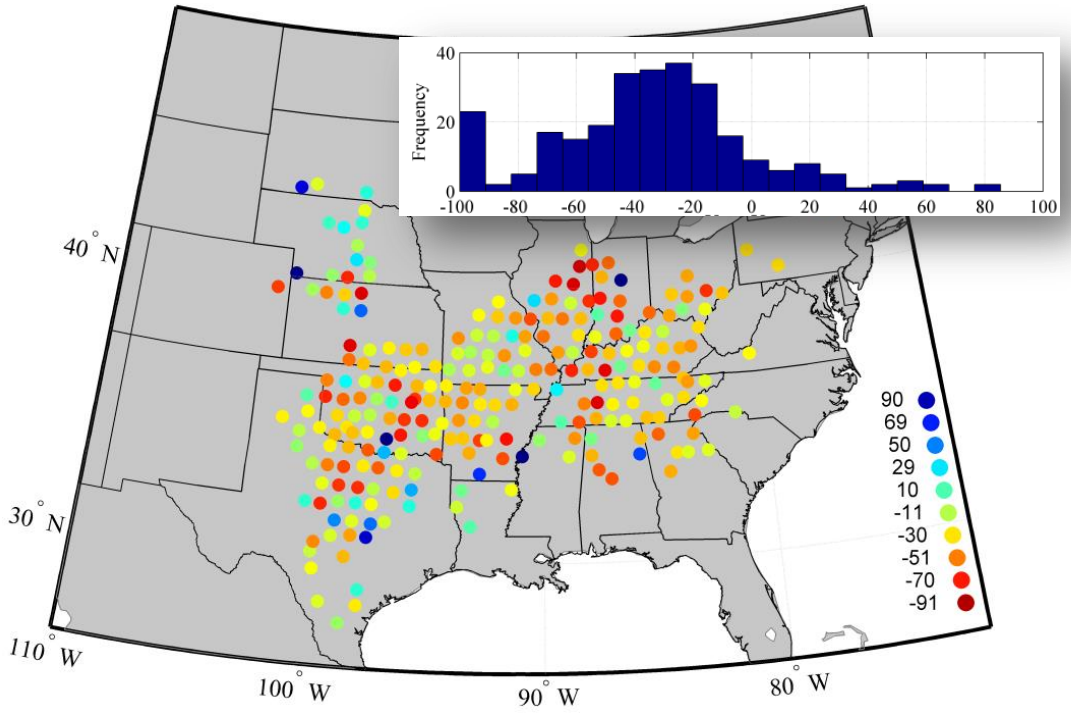

Figure 26. Comparison of shear-wave velocities (VS,T-Ave) obtained from this study with those from Ni and Somerville et al. (2012). The plotted values are percentage of different from Ni and Somerville (2013) values reported at 276 stations common between the two. The histogram shows that the majority of data are about 30 percent lower than those predicted by Ni and Somerville (2013).

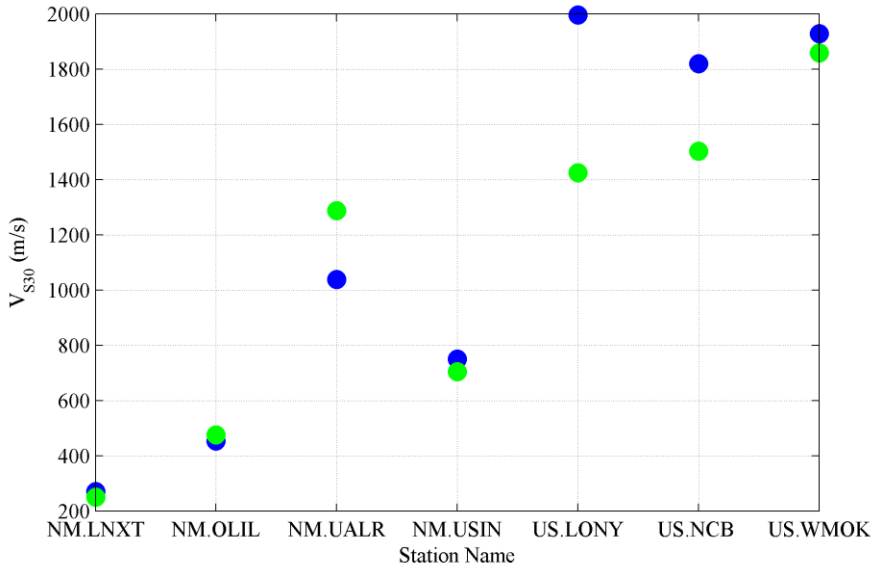

Figure 27. Comparison of shear-wave velocities acquired in this study with the measured values from Kim et al. (2016).

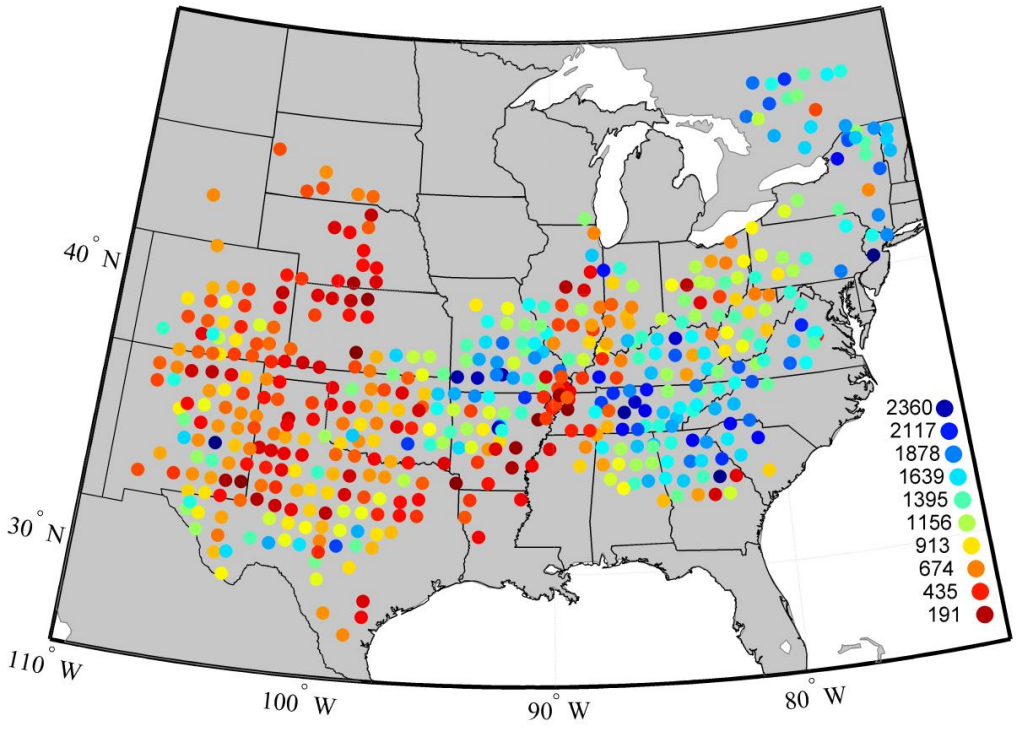

Figure 28. Arithmetic average of shear wave velocities $V_{S,Ave}$ (m/s) across the CEUS.

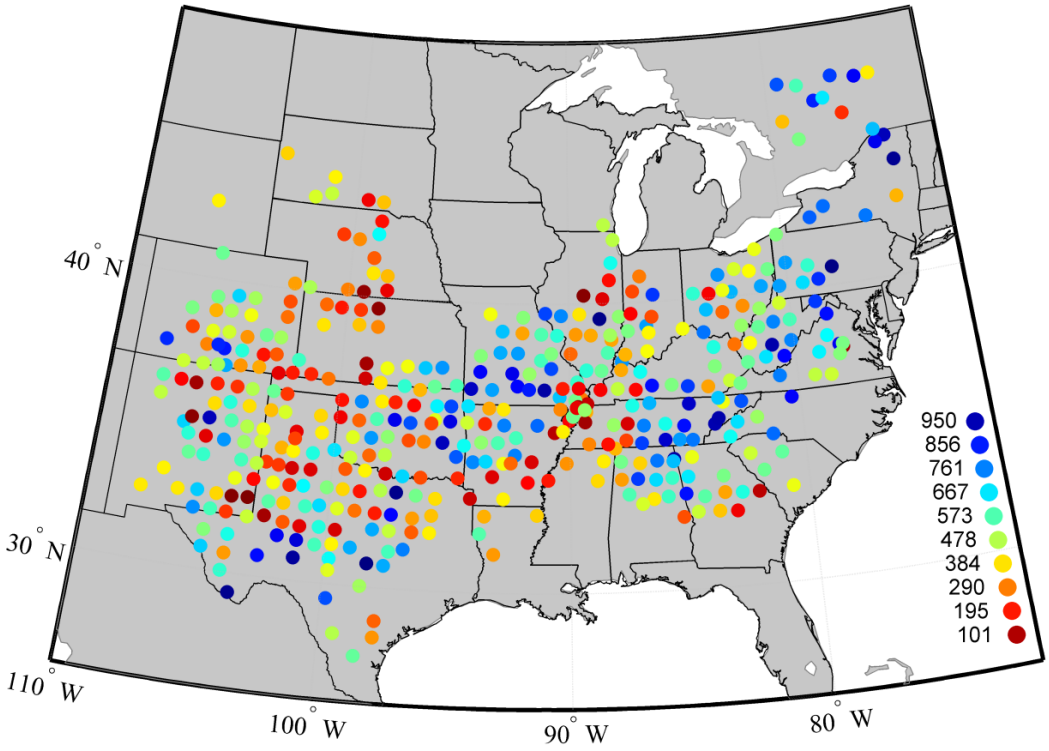

Figure 29. Time-averaged shear wave velocity (m/s) in upper 30 meters (V_{S30}) across the CEUS.

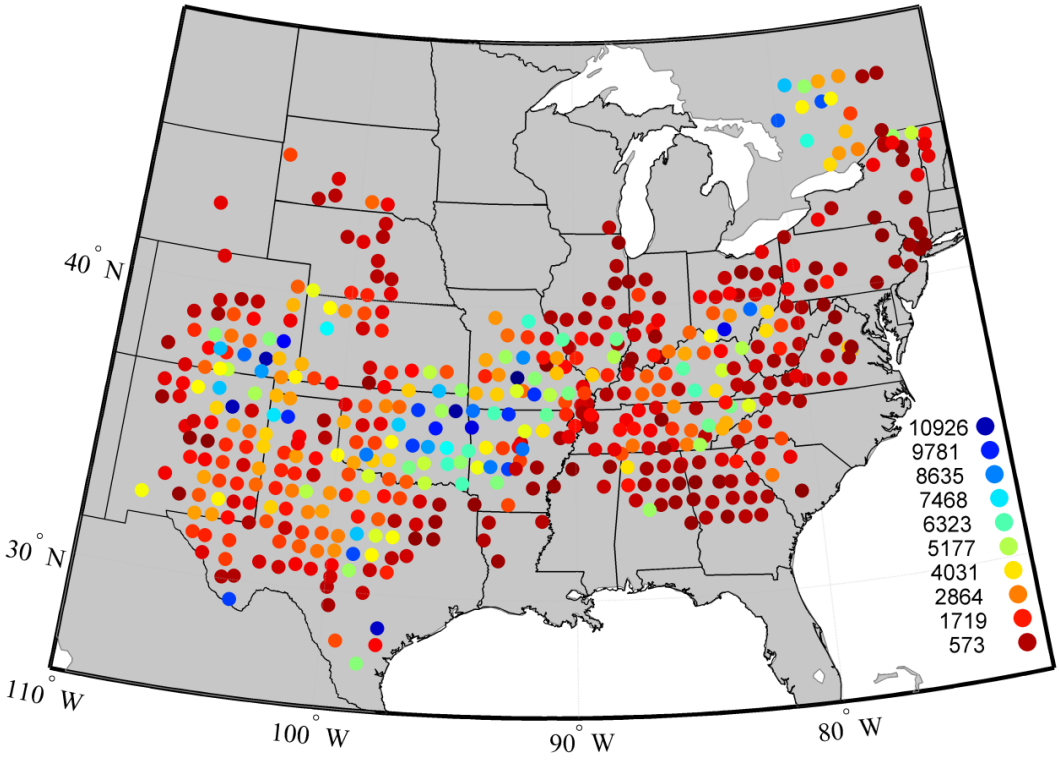

Figure 30. Average of geometric mean of SNR values (SNR_{Ave})from recorded earthquakes across the CEUS.

Table 6. Shear wave velocity parameters $V_{S,T\text{-}Ave}$, $V_{S,Ave}$, and V_{S30} along with SNR and inversion SPF.

*	Station	$V_{S,T\text{-}Ave}$	$V_{S,\,Ave}$	V_{S30}	SNR_{Ave}	*SPF* %
1	CPCT	1906	1715	1128	677	89
2	FPAL	1696	1705	967	911	79
3	SWET	1382	1505	929	1036	85
4	UOM1	1748	1534	1114	759	87
5	UOM2	331	436	86	3522	21
6	UOM3	707	3794	#N/A	8999	28
7	UOM4	1491	1525	892	3650	81
8	TKL	1713	1493	954	3436	96
9	TX31	897	957	984	9424	89
10	CCM	1132	1289	583	140	62
11	SSPA	1438	1483	995	683	81
12	WCI	1346	1363	#N/A	254	82
13	WVT	2427	2032	1011	1345	79
14	ACCN	2368	1954	2016	1179	97
15	BMNY	1176	1236	946	5458	85
16	BRNY	1936	2698	1693	315	91

17	FLET	1918	1708	1454	1557	98
18	FRNY	2096	1835	1613	4960	97
19	HBVT	2141	1681	1358	1146	93
20	HCNY	854	691	341	446	69
21	KSPA	1574	1551	1118	221	88
22	LUPA	#N/A	3719	#N/A	448	95
23	MCVT	2274	1737	1442	1174	100
24	MMNY	1412	1225	780	546	93
25	MSNJ	2903	2798	2591	289	98
26	MVL	2333	1893	1268	301	97
27	NCB	2095	2204	1599	2174	97
28	NPNY	1786	1859	1356	379	93
29	ODNJ	1852	1530	1085	383	94
30	PAL	1788	1850	1037	156	85
31	PANJ	2256	2482	1670	366	94
32	POTS	1787	1843	896	678	76
33	PTN	2093	1997	1025	556	94
34	WCNY	2917	2176	1714	1271	99
35	WVNY	1040	1052	794	1244	66
36	BLO	839	812	733	1628	67
37	CGM3	1554	1908	597	1195	81
38	CLTN	2843	2314	1968	185	93
39	FVM	2091	1706	1193	1537	95
40	GLAT	295	336	335	976	26
41	GNAR	352	426	171	1563	50
42	HALT	82	96	89	638	37
43	HBAR	78	91	110	489	47
44	HENM	406	302	288	817	34
45	HICK	228	333	119	#N/A	77
46	LNXT	998	3602	#N/A	629	27
47	LPAR	372	503	397	1189	28
48	MGMO	2499	2405	880	2625	70
49	OLIL	355	499	328	515	53
50	PBMO	894	1270	700	2237	63
51	PENM	187	297	96	#N/A	84
52	PLAL	765	768	344	2293	64
53	PVMO	182	148	152	502	49
54	SIUC	1400	1518	587	721	66
55	SLM	1372	1561	1323	587	82
56	UALR	1038	884	760	2128	68
57	USIN	829	964	742	401	71
58	X102	1452	1551	583	628	73
59	X201	2095	2106	1514	1337	93
60	X301	1597	2333	1061	1351	85

61	121A	554	548	390	4412	74
62	123A	457	485	391	264	63
63	124A	814	705	692	2371	63
64	125A	640	749	374	4220	45
65	126A	106	160	60	966	56
66	127A	83	92	56	1298	48
67	128A	711	634	564	3791	73
68	129A	467	474	362	1644	42
69	130A	676	788	589	2936	63
70	131A	870	890	678	3236	51
71	133A	369	282	279	1639	59
72	134A	490	541	197	2440	50
73	135A	778	1025	881	602	59
74	136A	395	394	319	953	35
75	137A	420	374	353	309	54
76	140A	400	483	337	560	64
77	143A	346	361	366	639	31
78	151A	762	814	246	244	83
79	152A	1351	1331	459	624	35
80	153A	491	742	356	294	62
81	154A	192	272	162	684	49
82	155A	827	1082	1353	602	43
83	224A	900	875	749	3246	59
84	225A	554	913	581	3200	42
85	226B	355	376	224	1532	77
86	227A	675	614	459	559	55
87	228A	118	189	90	2286	48
88	229A	210	254	256	832	60
89	230A	224	346	148	1988	42
90	231A	836	862	616	2386	51
91	232A	275	218	136	2862	36
92	233A	1030	1048	1011	7903	52
93	234A	949	1012	723	4749	58
94	236A	368	391	260	192	32
95	237A	495	488	396	307	76
96	240A	600	568	569	589	69
97	324A	1293	1225	1072	1984	42
98	325A	832	933	524	1813	43
99	326A	661	758	624	1949	72
100	329A	1004	1091	891	2080	69
101	330A	808	927	918	2397	70
102	331A	810	979	583	2719	75
103	332A	673	797	401	3048	69
104	333A	1084	1023	720	9299	86

105	334A	1727	1763	1242	4262	67
106	335A	964	910	583	700	61
107	336A	832	815	764	917	63
108	341A	389	360	315	343	62
109	425A	1296	1209	691	1092	65
110	426A	657	643	318	2107	71
111	428A	1249	1392	874	947	63
112	429A	1791	1773	1208	889	73
113	430A	938	1016	973	1366	68
114	431A	1762	1633	1258	1218	85
115	432A	678	677	640	1355	62
116	433A	2543	2026	1335	5400	99
117	434A	1543	1343	997	800	95
118	435B	800	805	722	1783	52
119	526A	1039	822	599	556	62
120	527A	1335	1658	1156	560	70
121	532A	1479	1309	1324	667	61
122	534A	775	897	497	796	85
123	632A	1149	1034	809	462	77
124	735A	273	284	265	10742	63
125	833A	693	716	478	2278	75
126	835A	382	352	310	1423	67
127	934A	714	692	554	5682	59
128	ABTX	892	877	440	#N/A	58
129	D51A	1909	1912	805	7934	75
130	D52A	1507	1527	578	5509	59
131	D53A	2491	2063	1164	3339	92
132	D54A	1703	1375	825	3166	95
133	D55A	1844	1597	888	393	85
134	D56A	1177	1510	394	352	67
135	E52A	2202	1982	1257	4218	96
136	E53A	1613	1368	854	9192	80
137	E54A	1468	1271	665	4266	79
138	F51A	2234	1915	1202	9119	90
139	F52A	991	1127	350	#N/A	44
140	F55A	613	533	215	2093	64
141	G53A	1618	1765	531	6792	80
142	G55A	1935	1652	1099	3601	83
143	G57A	1952	1809	707	339	78
144	H25A	485	545	369	2161	24
145	H55A	1871	1671	1150	3228	93
146	H58A	1747	1373	1039	230	83
147	I28A	592	708	402	1023	50
148	J27A	541	543	446	594	30

149	J28A	607	543	463	653	61
150	J31A	407	615	353	1296	49
151	K22A	603	695	399	1157	80
152	K31A	238	231	186	805	41
153	K43A	1278	1251	471	672	82
154	KMSC	2000	1924	782	2221	93
155	KSCO	380	353	277	1255	43
156	L29A	324	296	225	637	33
157	L30A	325	354	303	1122	22
158	L31A	717	585	642	580	37
159	L44A	716	681	472	286	60
160	L53A	920	953	525	413	43
161	M44A	1730	1706	627	550	68
162	M52A	817	676	429	1138	55
163	MSTX	316	277	226	#N/A	64
164	N23A	719	738	547	1070	73
165	N31A	381	393	388	661	69
166	N32A	363	375	347	662	45
167	N44A	391	354	183	301	40
168	N45A	678	2154	#N/A	287	48
169	N46A	1098	1477	288	515	62
170	N50A	1124	1152	747	809	54
171	N51A	821	742	445	233	34
172	N52A	740	665	413	419	42
173	N53A	1071	958	541	473	65
174	N54A	1166	1030	736	1353	64
175	N55A	1199	1194	599	247	90
176	O28A	452	489	486	4550	22
177	O30A	303	375	291	1713	45
178	O31A	113	163	73	1790	44
179	O32A	331	292	154	1167	67
180	O43A	124	193	65	494	34
181	O44A	150	290	143	651	38
182	O47A	1169	1165	834	477	44
183	O49A	1013	982	602	1362	58
184	O50A	296	216	167	1039	55
185	O51A	1072	1142	714	515	34
186	O52A	1057	1379	1368	972	32
187	O53A	1232	1100	729	1029	69
188	O54A	1474	1478	734	1221	55
189	O55A	995	920	675	300	66
190	O56A	1393	1162	840	1648	91
191	P23A	742	789	537	742	75
192	P24A	864	740	685	511	67

193	P25A	570	505	494	747	86
194	P27A	278	226	244	3497	55
195	P29A	284	293	270	4317	61
196	P30A	245	284	193	3013	57
197	P31A	339	235	226	2249	50
198	P32A	96	127	71	1216	51
199	P38A	755	929	421	3123	51
200	P40A	1018	1005	521	6593	53
201	P41A	1725	1568	819	488	60
202	P42A	1210	1470	754	667	56
203	P43A	553	509	387	423	49
204	P44A	558	1184	991	915	35
205	P45A	335	644	514	526	68
206	P46A	388	591	173	820	44
207	P47A	589	677	243	1236	68
208	P50A	1171	1260	705	2382	56
209	P51A	394	313	269	3101	45
210	P52A	535	525	308	8900	49
211	P53A	785	867	503	3904	63
212	P54A	877	666	450	650	40
213	P55A	875	680	#N/A	490	71
214	P56A	1672	1477	830	234	84
215	Q22A	906	916	532	751	74
216	Q23A	538	543	340	412	52
217	Q24A	1013	992	489	2321	88
218	Q25A	554	484	420	1427	95
219	Q29A	581	515	386	7260	58
220	Q31A	428	401	357	920	74
221	Q32A	360	374	298	1719	60
222	Q39A	1700	1543	701	2606	80
223	Q40A	1062	1135	326	2015	69
224	Q41A	1257	1243	572	1054	76
225	Q42A	996	1270	609	6205	69
226	Q43A	482	531	315	1599	56
227	Q44A	451	531	330	865	61
228	Q45A	689	743	496	5959	48
229	Q46A	540	668	531	874	52
230	Q47A	493	789	403	343	62
231	Q49A	1092	1103	418	2496	77
232	Q50A	1565	1448	775	4303	77
233	Q51A	1220	1184	1169	10328	71
234	Q52A	1200	1324	506	#N/A	56
235	Q53A	1288	1390	551	3946	45
236	Q54A	645	875	760	2095	76

237	Q55A	1148	1139	579	846	80
238	Q57A	1665	1471	870	240	82
239	R22A	492	534	239	1878	61
240	R23A	603	568	434	5652	75
241	R24A	783	892	452	2703	94
242	R25A	492	445	312	2516	63
243	R26A	1027	1063	545	5672	73
244	R27A	543	610	497	10174	69
245	R38A	1369	1397	523	3335	77
246	R39A	1795	1652	720	5382	85
247	R40A	1744	1919	736	8485	84
248	R41A	1576	1419	1052	1638	76
249	R42A	1628	1597	527	3254	92
250	R43A	473	699	268	1776	88
251	R45A	865	887	575	5230	57
252	R46A	708	772	342	317	32
253	R47A	1461	1728	416	1675	69
254	R48A	1315	1450	1067	2702	70
255	R49A	1615	1645	1190	3351	73
256	R50A	2588	2303	1525	2355	87
257	R51A	1680	1567	618	1415	66
258	R52A	680	644	279	5186	55
259	R53A	1091	993	412	697	70
260	R54A	1511	1376	959	1729	91
261	R55A	997	843	759	709	76
262	R57A	1765	2104	646	324	62
263	R58B	1458	1551	533	272	71
264	S21A	1562	1452	845	449	83
265	S23A	364	320	296	1466	64
266	S24A	1127	1116	863	1773	82
267	S25A	829	917	611	8872	81
268	S26A	400	541	189	11023	66
269	S27A	528	616	256	3584	51
270	S28A	511	598	590	3472	90
271	S32A	73	74	89	954	64
272	S33A	837	797	423	1879	54
273	S34A	1194	1678	421	1482	63
274	S35A	947	1111	697	5047	48
275	S36A	997	1131	743	2306	76
276	S38A	1474	1244	885	1808	83
277	S39A	1941	1774	1041	3105	89
278	S40A	1994	1815	901	11521	80
279	S41A	1044	1080	505	5634	86
280	S42A	1969	1841	816	3632	90

281	S44A	1134	1377	607	3779	59
282	S45A	1103	1096	550	1807	81
283	S46A	469	462	330	1083	58
284	S47A	557	675	633	2438	57
285	S48A	1746	1423	1008	2023	88
286	S49A	1563	1592	1186	6188	90
287	S50A	1797	1978	1050	#N/A	63
288	S51A	927	764	526	4864	73
289	S52A	1459	1612	1197	753	55
290	S53A	711	918	551	1006	73
291	S54A	1179	1016	668	453	82
292	S55A	1633	1483	881	532	75
293	S57A	1670	1713	654	600	83
294	S58A	1301	1366	523	335	88
295	SFIN	660	875	241	2017	59
296	T22A	766	772	458	1048	73
297	T23A	636	585	466	2550	83
298	T24A	1067	915	722	5026	97
299	T24B	676	594	493	4297	85
300	T25A	704	503	314	#N/A	54
301	T26A	485	555	331	8329	80
302	T27A	290	459	151	3049	46
303	T28A	289	332	194	4204	69
304	T29A	232	246	206	2083	45
305	T30A	313	284	282	1488	51
306	T32A	263	527	131	243	59
307	T33A	695	654	389	1378	76
308	T34A	1234	1280	602	3759	81
309	T35A	630	578	343	#N/A	72
310	T36A	1046	1017	551	7952	59
311	T37A	1283	1327	577	5537	91
312	T38A	2571	2384	939	3480	88
313	T39A	2416	2349	732	3781	84
314	T40A	1993	1877	1045	4731	83
315	T41A	2011	1808	857	9582	83
316	T42A	1724	1486	964	5115	63
317	T43A	304	288	197	5845	83
318	T44A	411	549	166	2097	70
319	T45A	320	489	168	620	66
320	T46A	1816	2163	466	996	52
321	T47A	455	517	179	2562	43
322	T48A	2677	2539	872	2314	89
323	T49A	1724	1731	530	661	73
324	T50A	1247	1193	829	6367	65

325	T51A	802	739	325	3926	45
326	T52A	974	1646	460	746	57
327	T53A	1364	1252	538	636	88
328	T54A	2314	1966	1716	558	84
329	T55A	1438	1201	766	357	87
330	T56A	2585	3285	1626	755	89
331	T57A	1682	1949	467	830	78
332	T58A	1488	1557	456	945	77
333	TASO	1044	951	686	1219	76
334	TUL1	536	589	435	#N/A	65
335	U21A	627	590	566	1166	71
336	U22A	426	683	173	1367	51
337	U23A	196	259	89	4297	68
338	U24A	237	213	203	7869	63
339	U25A	240	302	219	#N/A	42
340	U26A	687	879	480	5277	40
341	U27A	740	703	549	3528	84
342	U28A	321	372	223	3183	42
343	U31A	231	315	188	1095	36
344	U32A	1130	1279	752	2313	45
345	U33A	741	700	395	2941	34
346	U34A	509	534	202	2572	53
347	U35A	253	308	178	9491	36
348	U36A	823	846	654	5346	74
349	U37A	1913	1691	814	11181	94
350	U38A	1800	1771	670	8805	84
351	U39A	1578	1843	327	6410	79
352	U40A	1179	1548	391	9604	66
353	U42A	2228	2059	1771	6084	69
354	U43A	271	464	299	1860	51
355	U44B	543	586	509	1521	65
356	U47A	2106	2085	625	1348	80
357	U48A	1997	1860	713	1038	83
358	U49A	2356	2155	1056	3066	97
359	U50A	1223	1228	933	579	60
360	U52A	1058	1271	421	5825	58
361	U53A	1773	1512	803	4652	90
362	U54A	1532	1544	1226	879	83
363	U55A	2226	1991	1267	676	93
364	U56A	1343	1343	886	484	81
365	V21A	598	531	471	333	70
366	V22A	1362	1506	1561	1123	75
367	V24A	506	731	380	3848	64
368	V25A	733	933	610	10946	78

369	V26A	365	498	383	892	48
370	V27A	359	401	350	7490	60
371	V28A	531	561	446	9694	49
372	V30A	528	515	373	489	35
373	V31A	308	345	162	3370	46
374	V32A	335	325	264	1025	46
375	V33A	692	724	575	1219	49
376	V34A	970	860	898	7792	99
377	V35A	624	835	807	#N/A	75
378	V36A	279	274	239	9858	76
379	V37A	1752	1547	907	#N/A	93
380	V38A	1165	1104	455	10454	84
381	V39A	449	521	211	#N/A	67
382	V40A	971	1048	763	#N/A	47
383	V41A	904	1214	1335	4574	46
384	V42A	1412	1445	785	4011	76
385	V46A	1478	1569	505	1541	83
386	V47A	383	574	137	1578	77
387	V48A	2411	2422	764	1343	59
388	V49A	2201	2233	627	1927	72
389	V50A	1952	1716	871	2524	76
390	V51A	1973	1599	1075	5965	91
391	V52A	1812	1596	959	3436	87
392	V53A	1826	1752	674	2384	95
393	V54A	1660	1735	502	1035	91
394	W23A	654	380	68	887	74
395	W24A	1045	1022	947	1520	69
396	W25A	484	615	572	3195	83
397	W26A	717	703	477	2478	64
398	W27A	485	696	424	3809	62
399	W29A	244	249	152	1404	55
400	W30A	326	376	398	644	27
401	W32A	748	645	437	2092	84
402	W33A	1043	907	739	2143	92
403	W34A	787	670	514	4293	85
404	W35A	319	317	245	9462	54
405	W36A	413	448	299	8257	65
406	W37A	1319	1360	553	6269	78
407	W37B	782	976	943	7124	45
408	W38A	1452	1423	634	6381	63
409	W39A	1278	1171	512	4160	87
410	W40A	1043	934	575	2109	69
411	W41A	1493	1467	1119	6877	85
412	W41B	1598	1513	1070	8812	83

413	W45A	411	441	295	1066	50
414	W46A	289	442	184	1171	62
415	W47A	801	798	234	2713	78
416	W48A	2370	2205	823	943	88
417	W49A	2253	2003	1318	481	87
418	W50A	1589	1490	737	2788	76
419	W51A	1998	1791	772	5311	89
420	W53A	874	3129	635	538	47
421	W54A	2387	2193	1397	878	95
422	WHTX	339	447	463	4382	53
423	X23A	1273	1307	607	236	62
424	X24A	265	369	149	155	48
425	X25A	498	724	741	1836	82
426	X26A	546	721	503	1768	79
427	X27A	559	538	452	3806	56
428	X28A	565	656	340	1837	36
429	X29A	670	768	402	3210	36
430	X30A	884	830	619	1502	40
431	X31A	1141	1193	670	4300	54
432	X32A	782	875	458	3295	65
433	X33A	341	707	268	3716	24
434	X34A	868	877	472	3863	92
435	X36A	283	2049	2381	4960	35
436	X37A	1747	1476	1261	6537	91
437	X38A	1430	1168	801	5563	94
438	X39A	1850	1663	756	4489	95
439	X40A	759	726	419	9377	68
440	X41A	284	299	267	813	52
441	X42A	104	125	140	428	39
442	X44A	381	302	309	140	84
443	X47A	1169	1588	538	4040	38
444	X48A	1034	1185	368	480	59
445	X49A	1897	1719	773	711	68
446	X50B	1638	1336	705	591	84
447	X51A	1420	1501	428	481	68
448	X52A	2264	2200	1558	1056	62
449	X53A	1631	1811	1052	1669	53
450	X54A	1535	1619	456	1012	87
451	X56A	2007	2178	555	1221	78
452	Y23A	1353	1670	551	1572	66
453	Y24A	591	703	595	1365	65
454	Y25A	1783	2474	1381	2038	67
455	Y26A	470	839	583	946	54
456	Y27A	575	665	470	3248	50

457	Y28A	292	283	225	1779	84
458	Y29A	260	327	133	1740	49
459	Y30A	274	336	142	855	75
460	Y32A	581	604	256	2210	66
461	Y33A	584	586	400	4799	58
462	Y34A	237	369	130	2280	47
463	Y35A	697	777	681	2435	66
464	Y36A	458	399	243	4988	34
465	Y38A	407	293	209	6408	55
466	Y40A	272	495	144	5759	83
467	Y42A	141	175	174	389	66
468	Y43A	317	368	193	247	71
469	Y46A	845	869	376	844	71
470	Y47A	812	748	319	1620	81
471	Y48A	1117	1011	827	509	72
472	Y49A	1382	1188	677	599	89
473	Y50A	1120	1188	594	185	44
474	Y51A	1671	1569	663	191	76
475	Y52A	2261	1899	1217	270	94
476	Y53A	1653	1644	534	508	91
477	Y54A	2383	2072	1187	813	97
478	Y55A	1664	1658	545	2771	80
479	Z22A	732	769	398	1316	56
480	Z24A	975	1215	1478	3259	49
481	Z25A	1092	1396	1436	2074	68
482	Z26A	656	727	428	1768	72
483	Z27A	341	399	179	2598	51
484	Z28A	475	434	418	1724	53
485	Z29A	286	320	211	2791	56
486	Z30A	724	912	647	5152	52
487	Z31A	1282	1443	524	3095	57
488	Z32A	720	799	374	1668	63
489	Z33A	268	267	191	3579	59
490	Z34A	693	724	477	1551	69
491	Z36A	988	1141	538	984	56
492	Z37A	606	583	382	440	56
493	Z39A	90	83	125	219	55
494	Z41A	404	402	398	2208	70
495	Z48A	1259	1083	574	772	50
496	Z49A	873	1435	390	405	59
497	Z50A	1668	1764	590	354	84
498	Z51A	1476	1603	868	266	74
499	Z52A	1777	1699	564	607	97
500	Z53A	1290	1418	325	588	61

501	Z54A	1232	2454	618	569	48
502	Z55A	323	303	111	561	42
503	Z57A	879	864	428	167	69
504	ACSO	854	1138	426	1422	63
505	AMTX	369	341	234	1307	50
506	BINY	1514	1332	772	198	64
507	BLA	1532	1488	1111	1152	86
508	JCT	484	452	438	906	80
509	LONY	1996	1693	1135	1324	97
510	LRAL	924	975	447	5463	71
511	MIAR	1219	1043	681	8702	82
512	MNTX	1745	1502	1210	#N/A	97
513	NCB	1819	1379	981	295	99
514	SDCO	1492	1525	849	7947	96
515	TZTN	2015	1890	696	1565	93
516	WMOK	1927	1701	1261	8716	97

* Station number and seismic network color code based on the following color scheme:

ET	IM	IU	LD	NM	TA	US

Electronic Supplements

Downloaded earthquake recordings for ~3,000 earthquake and ~73,000 three-component recordings are available in SAC format, for each of the following cases

- **Database:**

  (1) Raw data downloaded from IRIS DMC
  (2) Instrument-corrected data
  (3) High-pass filtered data
  (4) Receiver functions
  (5) Inversion files and results

- **Scripts and Programs**
  (1) XML scripts to download data from IRIS using SOD software
  (2) Shell scripts to pre-process the data for the following tasks
    a. Formatting the folder structure
    b. Instrument response collection and correction
    c. Filter and SNR calculation
  (3) MATLAB scripts to pick arrival time using non-AR AIC algorithm and set header
  (4) MATLAB scripts for visual inspection, correction of arrival time with respect to non-AR AIC pick/P wave phases from Taup, and preparing observed receiver functions.
  (5) MATLAB scripts for visual inspection, synchronizing the receiver functions with respect to the one with highest SNR, and stacking
  (6) MATLAB script to generate various combinations for depth structure of the earth model.
  (7) Shell scripts for inversion of stacked receiver function for shear-wave velocity structure

Data and Resources

The waveforms used in this study include both radial and vertical components of motion from local earthquakes recorded at distances less than 300 km and distances more than the event depth. Events analyzed include 3000 earthquake and aftershocks (Fig. 1; Table 2). All waveforms were visually inspected and restricted to well-recorded earthquakes (2.5<M<4.5) with depth ≤ 30 km. Data used in this study were digitally recorded at broadband stations operated by the Transportable Array (TA), New Madrid (NM), CERI Southern Appalachian (ET), International Miscellaneous Stations (IM), United States (US), Global Seismograph (IU), United States National (US), Lamont-Doherty Cooperative (LD) seismic networks. Earthquake locations and magnitudes used in this study were obtained from the Incorporated Research Institutions for Seismology Data Management Center (IRIS DMC). All waveform data used in this study are archived and available for download from the IRIS DMC. Analysis software used includes Seismic Analysis Code (SAC; Goldstein et al., 2003; Goldstein and Snoke, 2005), MATLAB, CPS (Computer Programs in Seismology), and those developed by PIs at the University of Memphis, Department of Civil Engineering as a part of the NGA-East project. Additional data and resources were obtained from the following websites: Taup for identification of arrival phases http://www.seis.sc.edu/taup/ (last access 7/11/2015), SAC file format access in MATLAB http://web.utah.edu/thorne/software.html (last access 7/11/2015). Ground motion data were automatically downloaded using Standing Order of Data software (SOD). All three components of the waveforms are utilized in the analysis and only those stations were selected that simultaneously possessed components in three directions. Correcting for the instrument response was performed using SAC software.

References

Akaike, H. (1973). Information theory and an extension of the maximum likelihood principle, *2nd Intermational Symposium on Information Theory*, B. Petrov and F. Csaki (Editors), Budapest Akademiai Kiado, 267–281

Aki, K., and P. G. Richards (2002). *Quantitative Seismology*, Second Ed., University Science Books, Sausalito, California, ISBN 0-935702-96-2

Aster, R. C., B. Borchers, and C. H. Thurber (2013). *Parameter estimation and inverse problems*, Elsevier, Amsterdam, 2nd edition.

Chen, K., J. Chiu, and Y. Yang (1996). Shear-wave velocity of the sedimentary basin in the upper Mississippi embayment using S-to-P converted waves, *Bull. Seismol. Soc. Am.*, 86, 848–856.

Conn, A. (2013). *Q Models for Lg Wave Attenuation in the Central United States*, Master's Thesis, Virginia Polytechnic Institute and State University.

Crotwell, H. P., T. J. Owens, and J. Ritsema, The TauP Toolkit: Flexible seismic travel-time and ray-path utilities, *Seismol. Res. Lett.*, 70, 154–160, 1999.

Herrmann (2002). *An Overview of Synthetic Seismogram Computation*, Department of Earth and Atmospheric Sciences, Saint Louis University.

Hosseini, M. (2014). R*educing Uncertainties in the Velocities Determined By Inversion of Phase Velocity Dispersion Curves Using Synthetics Seismograms,* PhD Dissertation, The University of Memphis.

Hosseini, S. M., and S. Pezeshk. (2015). A Synthetic Study into the Nature and Solution of Nonuniqueness in Surface-Wave Inverse Problems, *Bull. Seismol. Soc. Am.,* 105, 3167-3179.

Hosseini, S. M., S. Pezeshk, A. Haji-Soltani, and M. Chapman. (2015). Investigation of Attenuation of the Fourier Amplitude in the Caribbean Region, *Bull. Seismol. Soc. Am.,* 105, 734-744.

Kim, B., Y. M. A. Hashash, E. M. Rathje, J. P. Stewart, S. Ni, P. G. Somerville, A. R. Kottke, W. J. Silva, and K. W. Campbell (2016). Subsurface Shear Wave Velocity Characterization Using *P*-Wave Seismograms in Central and Eastern North America, Earthquake Spectra, 32 (1).

Langston, C. A. (2003). Local earthquake wave propagation through Mississippi embayment sediments: I. Body wave phases and local site responses, *Bull. Seismol. Soc. Am.,* 93, 2664–2684.

Ligorria, J. P. and C. J. Ammon (1999). Iterative deconvolution and receiver-function estimation, *Bull. Seism. Soc. Am.,* 89, 1395-1400.

Maeda, N. (1985). A method for reading and checking phase times in auto-processing system of seismic wave data, *ZisinJishin* 38, 365–379

Ni, S. and P. Somerville (2013). Estimating site response by constraining shallow velocity structure with local P waves in the Central and Eastern United States, *U.S. Geological Survey*, Final Technical Report

Ni, s., Z. Li and P. Somerville (2014). Estimating Subsurface Shear Velocity with Radial to Vertical Ratio of Local P Waves, *Seismol. Res. Lett.*, 85(1), doi: 10.1785/0220130128

Ou, G. and R. Herrmann (1990). A statistical model for peak ground motion from local to regional distances, *Bull. Seism. Soc. Am.,* 80, 1,397-1,417.

Pujol, J. (2007). The solution of nonlinear inverse problems and the Levenberg-Marquardt method, *Geophysics* 72 W1-W16.

Zhang, H., C. Thurber, and C. Rowe (2003). Automatic P-Wave Arrival Detection and Picking with Multiscale Wavelet Analysis for Single-Component Recordings, *Bull. Seism. Soc. Am.,* 93(5), 1904–1912.

Appendix A

This appendix includes data used in the process of estimating the shear-wave velocity for CEUS seismic stations. We provide the plots for three sets of data for each station:

(1) Plots for radial and vertical time series that were used to generate receiver functions for different earthquake recordings
(2) Plot of receiver functions before and after synchronization for stacking into final observed receiver function representative of local shallow structure
(3) Plot of the match between observed and predicted receiver functions for highest SPF ratio where the predicted receiver functions are determined from the receiver function inversion process.
(4) Table of the receiver function inversion results provided for multiple scenarios with highest SPF. A maximum of 15 inversion results are provided, ranked by the SPF value.

The plots of radial and vertical time series show the theoretical arrival times predicted by IRIS (blue dashed line) and final arrival time (solid blue line). These plots might include P wave phase arrivals from Taup (thin dashed line with triangles at both ends). As explained in the processing section in the report, the time series are cut -1 and 5 seconds before and after the P wave arrival time and are de-convolved from each other to generate the receiver function. The receiver functions are then synchronized with the one with the highest SNR before stacking as presented in item 2 above.

Plot (item 3 in the list above) refers to the best match among all the scenarios explained in the inversion section of the report. Up to 15 scenarios with highest SPF are provided in a Table (item 4 in the list above). In this Table, the shear-wave velocity and thickness of three layers over a half-space are provided, along with the shear-wave parameters $V_{S,T\text{-}Ave}$, $V_{S,Ave}$, and V_{S30} as defined in the report. SPF for each scenario is provided in the right column of the Table. This appendix provides the data and plots for stations with SPF above 60 percent.

You can obtain a copy of Appendix A by sending your request to mehrdad.hosseini@aecom.com, or download it from https://sites.google.com/site/aecomseismology/